Scaling theory of continuum dislocation dynamics in three dimensions: Self-organized fractal pattern formation

Yong S. Chen [a], Woosong Choi [a], Stefanos Papanikolaou [b], Matthew Bierbaum [a], James P. Sethna [a,*]

[a] Laboratory of Atomic and Solid State Physics (LASSP), Clark Hall, Cornell University, Ithaca, NY 14853-2501, USA
[b] Department of Mechanical Engineering and Materials Science, Yale University, New Haven, CT 06520-8286, USA

A B S T R A C T

We focus on mesoscopic dislocation patterning via a continuum dislocation dynamics theory (CDD) in three dimensions (3D). We study three distinct physically motivated dynamics which consistently lead to fractal formation in 3D with rather similar morphologies, and therefore we suggest that this is a general feature of the 3D collective behavior of geometrically necessary dislocation (GND) ensembles. The striking self-similar features are measured in terms of correlation functions of physical observables, such as the GND density, the plastic distortion, and the crystalline orientation. Remarkably, all these correlation functions exhibit spatial power-law behaviors, sharing a single underlying universal critical exponent for each type of dynamics.

© 2013 Elsevier Ltd. All rights reserved.

1. Introduction

Dislocations in plastically deformed crystals, driven by their long-range interactions, collectively evolve into complex heterogeneous structures where dislocation-rich cell walls or boundaries surround dislocation-depleted cell interiors. These have been observed both in single crystals (Kawasaki and Takeuchi, 1980; Mughrabi et al., 1986; Schwink, 1992) and polycrystals (Ungár et al., 1986) using transmission electron microscopy (TEM). The mesoscopic cellular structures have been recognized as scale-free patterns through fractal analysis of TEM micrographs (Gil Sevillano et al., 1991; Gil Sevillano, 1993; Hähner et al., 1998; Zaiser et al., 1999), Fig. 1(a). The complex collective behavior of dislocations has been a challenge for understanding the underlying physical mechanisms responsible for the development of emergent dislocation morphologies.

Complex dislocation microstructures, as an emergent mesoscale phenomenon, have been previously modeled using various theoretical and numerical approaches (Ananthakrishna, 2007). Discrete dislocation dynamics (DDD) models have provided insights into the dislocation pattern formations: parallel edge dislocations in a two-dimensional system evolve into 'matrix structures' during single slip (Bakó et al., 1999), and 'fractal and cell structures' during multiple slip (Bakó et al., 2007; Bakó et al., 2007); random dislocations in a three-dimensional system self-organize themselves into microstructures through junction formation, cross-slip, and short-range interactions (Madec et al., 2002; Gomez-Garcia et al., 2006). However, DDD simulations are limited by the computational challenges on the relevant scales of length and strain. Beyond these micro-scale descriptions, CDD has also been used to study complex dislocation structures. Simplified reaction–diffusion models have described persistent slip bands (Walgraef and Aifantis, 1985), dislocation cellular structures during multiple
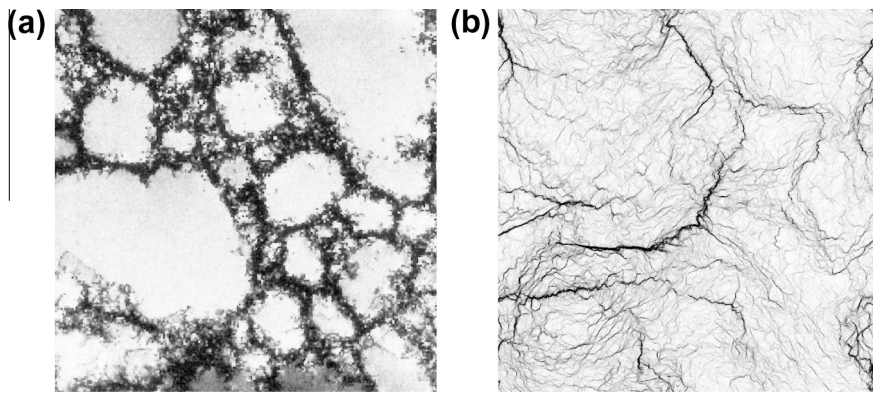
Fig. 1. Experimental and simulated dislocation cellular structures. In (a), a typical TEM micrograph at a micron scale is taken from a Cu single crystal after [100] tensile deformation to a stress of 76.5 MPa (Hähner et al., 1998); in (b), a simulated GND density plot is shown. Note the striking morphological similarity between theory and experiment.

slip (Hähner, 1996), and dislocation vein structures (Saxlová et al., 1997). Stochasticity in CDD models (Hähner et al., 1998; Bakó et al., 1999; Groma and Bakó, 2000) or in the splittings and rotations of the macroscopic cells (Pantleon, 1996; Pantleon, 1998; Sethna et al., 2003) have been suggested as an explanation for the formation of organized dislocation structures. The source of the noise in these stochastic theories is derived from either extrinsic disorder or short-length-scale fluctuations.

In a recent manuscript (Chen et al., 2010), we analyzed the behavior of a grossly simplified continuum dislocation model for plasticity (Acharya, 2001; Roy and Acharya, 2005; Acharya and Roy, 2006; Limkumnerd and Sethna, 2006; Chen et al., 2010) – a physicist's 'spherical cow' approximation designed to explore the minimal ingredients necessary to explain key features of the dynamics of deformation. Our simplified model ignores many features known to be important for cell boundary morphology and evolution, including slip systems and crystalline anisotropy, dislocation nucleation, lock formation and entanglement, line tension, geometrically unnecessary forest dislocations, etc. However, our model does encompass a realistic order parameter field (the Nye-Kröner dislocation density tensor (Nye, 1953; Kröner, 1958) embodying the GNDs), which allows detailed comparisons of local rotations and deformations, stress, and strain. It is not a realistic model of a real material, but it is a model material with a physically sensible evolution law. Given these simplifications, our model exhibited a surprisingly realistic evolution of cellular structures (Fig. 1(b)). We analyzed these structures in two-dimensional simulations (full three-dimensional rotations and deformations, but uniform along the z-axis) using both the fractal box counting method (Gil Sevillano et al., 1991; Gil Sevillano, 1993; Hähner et al., 1998; Zaiser et al., 1999) and the single-length-scale scaling methods (Hughes et al., 1997; Hughes et al., 1998; Mika and Dawson, 1999; Hughes and Hansen, 2001) used in previous theoretical analyses of experimental data. Our model qualitatively reproduced the self-similar, fractal patterns found in the former, and the scaling behavior of the cell sizes and misorientations under strain found in the latter (power-law refinement of the cell sizes, power-law increases in misorientations, and scaling collapses of the distributions).

There are many features of real materials which are not explained by our model. We do not observe distinctions between 'geometrically necessary' and 'incidental' boundaries, which appear experimentally to scale in different ways. The fractal scaling observed in our model may well be cut off or modified by entanglement, slip-system physics, quantization of Burgers vector (Kuhlmann-Wilsdorf, 1985) or anisotropy – we cannot predict that real materials should have fractal cellular structures; we only observe that our model material does so naturally. Our spherically symmetric model obviously cannot reproduce the dependence of morphological evolution on the axis of applied strain (and hence the number of activated slip systems); indeed, the fractal patterns observed in some experiments (Hähner et al., 1998; Zaiser et al., 1999) could be associated with the high-symmetry geometry they studied (Wert et al., 2007; Hansen et al., 2011). While many realistic features of materials that we ignore may be important for cell-structure formation and evolution, our model gives clear evidence that these features are not essential to the formation of cellular structures when crystals undergo plastic deformation.

In this longer manuscript, we provide an in-depth analysis of three plasticity models. We show how they (and more traditional models) can be derived from the structures of the broken symmetries and order parameters. We extend our simulations to 3D, where the behavior is qualitatively similar with a few important changes. Here we focus our attention on relaxation (rather than strain), and on correlation functions (rather than fractal box counting or cell sizes and misorientations).

Studying simplified 'spherical cow' models such as ours is justified if they capture some key phenomenon, providing a perspective or explanation for the emergent behavior. Under some circumstances, these simplified models can capture the long-wavelength behavior precisely – the model is said to be in the same universality class as the observed behavior (Sethna, 2006, Chapter 12). The Ising model for magnetism, two-fluid criticality, and order–disorder transitions; self-organized critical models for magnetic Barkhausen noise (Sethna et al., 2001; Durin and Zapperi, 2006) and dislocation avalanches (Zaiser, 2006) all exhibit the same type of emergent scale-invariant behavior as observed in some experimental cellular structures (Hähner et al., 1998). For all of these systems, 'spherical cow' models provide quantitative experimental predictions of

all phenomena on long length and time scales, up to overall amplitudes, relevant perturbations, and corrections to scaling. Other experimental cellular structures (Hughes et al., 1998) have been interpreted in terms of scaling functions with a characteristic scale, analogous to those seen in crystalline grain growth. Crystalline grain growth also has a 'universal' description, albeit one which depends upon the entire anisotropic interfacial energy and mobility (Rutenberg and Vollmayr-Lee, 1999) (and not just temperature and field).[1] We are cautiously optimistic that a model like ours (but with metastability and crystalline) could indeed describe the emergent complex dislocation structures and dynamics in real materials. Indeed, recent work on dislocation avalanches suggests that even the yield stress may be a universal critical point (Friedman et al., 2012).

Despite universality, we must justify and explain the form of the CDD model we study. In Section 2 we take the continuum, 'hydrodynamic' limit approach, traditionally originating with Landau in the study of systems near thermal equilibrium (clearly not true of deformed metals!). All degrees of freedom are assumed slaves to the order parameter, which is systematically constructed from conserved quantities and broken symmetries (Martin, 1968; Forster, 1975; Hohenberg and Halperin, 1977) – this is the fundamental tool used in the physics community to derive the diffusion equation, the Navier–Stokes equation, and continuum equations for superconductors, superfluids, liquid crystals, etc. Rickman and Viñals (1997) have utilized this general approach to generate CDD theories, and in Section 2 we explain how our approach differs from theirs.

In Section 3 we explore the validity of several approximations in our model, starting in the engineering language of state variables. Here local equilibration is not presumed; the state of the system depends in some arbitrarily complex way on the history. Conserved quantities and broken symmetries can be supplemented by internal state variables – statistically stored dislocations (SSDs), yield surfaces, void fractions, etc., whose evolution laws are judged according to their success in matching experimental observations. (Eddy viscosity theories of turbulence are particular successful examples of this framework.) The 'single-velocity' models we use were originally developed by Acharya et al. (Acharya, 2001; Roy and Acharya, 2005), and we discuss their microscopic derivation (Acharya, 2001) and the correction term L^p resulting from coarse-graining and multiple microscopic velocities (Acharya and Roy, 2006). This term is usually modeled by the effects of SSDs using crystal plasticity models. We analyze experiments to suggest that ignoring SSDs may be justified on the length-scales needed in our modeling. However, we acknowledge the near certainty that Acharya's L^p will be important – the true coarse-grained evolution laws will incorporate multiple velocities. Our model should be viewed as a physically sensible model material, not a rigorous continuum limit of a real material.

In this manuscript, we study fractal cell structures that form upon relaxation from randomly deformed initial conditions (Section 4.2). One might be concerned that relaxation of a randomly imposed high-stress dislocation structure (an instantaneous hammer blow) could yield qualitatively different behavior from realistic deformations, where the dislocation structures evolve continuously as the deformation is imposed. In Section 4.2 we note that this alternative 'slow hammering' gives qualitatively the same fractal dislocation patterns. Also, the resulting cellular structures are qualitatively very similar to those we observe under subsequent uniform external strain (Chen et al., 2010), except that the relaxed structures are statistically isotropic. We also find that cellular structures form immediately at small deformations. Cellular structures in real materials emerge only after significant deformation; presumably this feature is missing in our model because our model has no impediment to cross-slip or multiple slip, and no entanglement of dislocations. This initial relaxation should not be viewed as annealing or dislocation creep. A proper description of annealing must include dislocation line tension effects, since the driving force for annealing is the reduction in total dislocation density – our dislocations annihilate when their Nye Burgers vector density cancels under evolution, not because of the dislocation core energies. Creep involves dislocation climb, which (for two of our three models) is forbidden.

We focus here on correlation functions, rather than the methods used in previous analyses of experiments. Correlation functions have a long, dignified history in the study of systems exhibiting emergent scale invariance – materials at continuous thermodynamic phase transitions (Chaikin and Lubensky, 1995), fully developed turbulence (L'vov, 1991; Choi et al., 2012b; Salman and Truskinovsky, 2012), and crackling noise and self-organized criticality (Sethna et al., 2001). We study not only numerical simulations of these correlations, but provide also extensive analysis of the relations between the correlation functions for different physical quantities and their (possibly universal) power-law exponents. The decomposition of the system into cells (needed for the cell-size and misorientation distribution analyses (Hughes et al., 1997; Hughes et al., 1998; Mika and Dawson, 1999; Hughes and Hansen, 2001)) demands the introduction of an artificial cutoff misorientation angle, and demands either laborious human work or rather sophisticated numerical algorithms (Chen et al., 2012). These sections of the current manuscript may be viewed both as a full characterization of the behavior of our simple model, and as an illustration of how one can use correlation functions to analyze the complex morphologies in more realistic models and in experiments providing 2D or 3D real-space data. We believe that analyses that explicitly decompose structures into cells remain important for systems with single changing length-scale: grain boundary coarsening should be studied both with correlation functions and with explicit studies of grain shape and geometry evolution, and the same should apply to cell-structure models and experiments that are not fractal. But our model, without such an intermediate length-scale, is best analyzed using correlation functions.

Our earlier work (Chen et al., 2010) focused on 2D. How different are our predictions in 3D? In this paper, we explore three different CDDs that display similar dislocation fractal formation in 3D and confirm analytically that correlation functions of the GND density, the plastic distortion, and the crystalline orientation, all share a single underlying critical exponent,

---

[1] See, however, Kacher et al. (2011) for experimental observations of bursty grain growth is incompatible with these theories.

up to exponent relations, dependent only on the type of dynamics. Unlike our 2D simulations, where forbidding climb led to rather distinct critical exponents, all three dynamics in 3D share quite similar scaling behaviors.

We begin our discussion in Section 2.1 by defining the various dislocation, distortion, and orientation fields. In Section 2.2, we derive standard local dynamical evolution laws using traditional condensed matter approaches, starting from both the non-conserved plastic distortion and the conserved GND densities as order parameters. Here, we also explain why these resulting dynamical laws are inappropriate at the mesoscale. In Section 2.3, we show how to extend this approach by defining appropriate constitutive laws for the dislocation flow velocity to build novel dynamics (Landau and Lifshitz, 1970). There are three different dynamics we study: i) isotropic climb-and-glide dynamics (CGD) (Acharya, 2001; Acharya, 2003; Acharya, 2004; Roy and Acharya, 2005; Limkumnerd and Sethna, 2006), ii) isotropic glide-only dynamics, where we define the part of the local dislocation density that participates in the local *mobile dislocation population*, keeping the local volume conserved at all times (GOD-MDP) (Chen et al., 2010), iii) isotropic glide-only dynamics, where glide is enforced by a *local vacancy pressure* due to a co-existing background of vacancies that have an infinite energy cost (GOD-LVP) (Acharya and Roy, 2006). All three types of dynamics present physically valid alternative approaches for deriving a coarse-grained continuum model for GNDs. In Section 3, we explore the effects of coarse-graining, explain our rationale for ignoring SSDs at the mesoscale, and discuss the single-velocity approximation we use. In Section 4, we discuss the details of numerical simulations in both two and three dimensions, and characterize the self-organized critical complex patterns in terms of correlation functions of the order parameter fields. In Section 5, we provide a scaling theory, derive relations among the critical exponents of these related correlation functions, study the correlation function as a scaling function of coarse-graining length scale, and conclude in Section 6.

In addition, we provide extensive details of our study in Appendices. In A, we collect useful formulas from the literature relating different physical quantities within traditional plasticity, while in B we show how functional derivatives and the dissipation rate can be calculated using this formalism, leading to our proof that our CDDs are strictly dissipative (lowering the appropriate free energy with time). In C, we show the flexibility of our CDDs by extending our dynamics: In particular, we show how to add vacancy diffusion in the structure of CDD, and also, how external disorder can be in principle incorporated (to be explored in future work). In D, we elaborate on numerical details – we demonstrate the statistical convergence of our simulation method and also we explain how we construct the Gaussian random initial conditions. Finally, in E, we discuss the scaling properties of several correlation functions in real and Fourier spaces, including the strain-history-dependent plastic deformation and distortion fields, the stress-stress correlation functions, the elastic energy density spectrum, and the stressful part of GND density.

2. Continuum models

2.1. Order parameter fields

2.1.1. Conserved order parameter field

A dislocation is the topological defect of a crystal lattice. In a continuum theory, it can be described by a coarse-grained variable, the GND density,[2] (also called the net dislocation density or the Nye-Kröner dislocation density), which can be defined by the GND density tensor

$$\rho(\mathbf{x}) = \sum_\alpha (\hat{\mathbf{t}}^\alpha \cdot \hat{\mathbf{n}})\hat{\mathbf{n}} \otimes \mathbf{b}^\alpha \delta(\mathbf{x} - \xi^\alpha), \tag{1}$$

so

$$\rho_{km}(\mathbf{x}) = \sum_\alpha \hat{t}_k^\alpha b_m^\alpha \delta(\mathbf{x} - \xi^\alpha), \tag{2}$$

measuring the sum of the net flux of dislocations α located at ξ, tangent to $\hat{\mathbf{t}}$, with Burgers vector $\mathbf{b}$, in the neighborhood of $\mathbf{x}$, through an infinitesimal plane with the normal direction along $\hat{\mathbf{n}}$, seen in Fig. 2. In the continuum, the discrete sum of line singularities in Eqs. (1) and (2) is smeared into a continuous (nine-component) field, just as the continuum density of a liquid is at root a sum of point contributions from atomic nuclei.

Since the normal unit pseudo-vector $\hat{\mathbf{n}}$ is equivalent to an antisymmetric unit bivector $\widehat{E}$, $\widehat{E}_{ij} = \varepsilon_{ijk}\hat{n}_k$, we can reformulate the GND density as a three-index tensor

$$\varrho(\mathbf{x}) = \sum_\alpha (\hat{\mathbf{t}}^\alpha \cdot \hat{\mathbf{n}})\widehat{E} \otimes \mathbf{b}^\alpha \delta(\mathbf{x} - \xi^\alpha), \tag{3}$$

so

$$\varrho_{ijm}(\mathbf{x}) = \sum_\alpha (\hat{\mathbf{t}}^\alpha \cdot \hat{\mathbf{n}})\widehat{E}_{ij} b_m^\alpha \delta(\mathbf{x} - \xi^\alpha), \tag{4}$$

---

[2] Dislocations which cancel at the macroscale may be geometrically necessary at the mesoscale. See Section 3 for our rationale for not including the effects of SSDs (whose Burgers vectors cancel in the coarse-graining process).
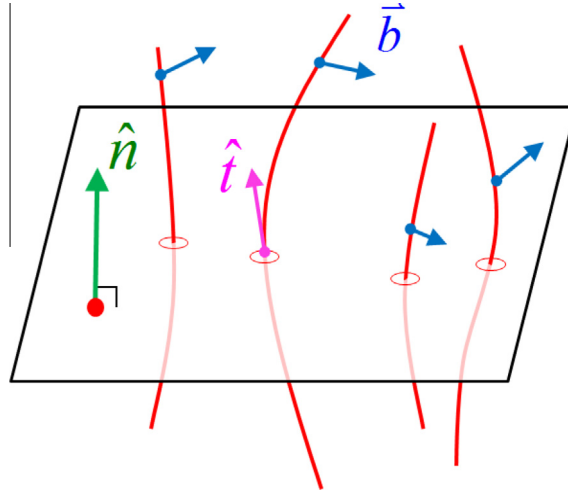
Fig. 2. Representation of the crystalline line defect—dislocation. Each curved line represents a dislocation line with the tangent direction $\hat{t}$, and the Burgers vector **b** which characterizes the magnitude and direction of the distortion to the lattice. The two-index GND density ρ_{km} (Nye, 1953; Kröner, 1958) (Eqs. 1 and 2) is the net flux of the Burgers vector density **b** along $\hat{\mathbf{e}}^{(m)}$ through an infinitesimal piece of a plane with normal direction $\hat{\mathbf{n}}$ along $\hat{\mathbf{e}}^{(k)}$. The three-index version ϱ_{ijm} (Eqs. 3 and 4) is the flux density through the plane along the axes $\hat{\mathbf{e}}^{(i)}$ and $\hat{\mathbf{e}}^{(j)}$, with the unit bivector $\widehat{E} = \hat{\mathbf{e}}^{(i)} \wedge \hat{\mathbf{e}}^{(j)}$.

measuring the same sum of the net flux of dislocations in the neighborhood of **x**, through the infinitesimal plane indicated by the unit bivector $\widehat{E}$. This three-index variant will be useful in Section 2.3.2, where we adapt the equations of Roy and Acharya (2005) and Limkumnerd and Sethna (2006) to forbid dislocation climb (GOD-MDP).

According to the definition of $\widehat{E}$, we can find the relation between ρ and ϱ

$$\varrho_{ijm}(\mathbf{x}) = \sum_\alpha (\hat{t}_l^\alpha \hat{n}_l)\varepsilon_{ijk}\hat{n}_k b_m^\alpha \delta(\mathbf{x} - \xi^\alpha) = \varepsilon_{ijk}\rho_{km}(\mathbf{x}). \tag{5}$$

It should be noted here that dislocations cannot terminate within the crystal, implying that

$$\partial_i \rho_{ij}(\mathbf{x}) = 0, \tag{6}$$

or

$$\varepsilon_{ijk}\partial_k \varrho_{ijl}(\mathbf{x}) = 0. \tag{7}$$

Within plasticity theories, the gradient of the total displacement field **u** represents the compatible total distortion field (Kröner, 1958; Kröner, 1981) $\beta_{ij} = \partial_i u_j$, which is the sum of the elastic and the plastic distortion fields (Kröner, 1958; Kröner, 1981), $\beta = \beta^{\mathrm{p}} + \beta^{\mathrm{e}}$. Due to the presence of dislocation lines, both β^{p} and β^{e} are incompatible, characterized by the GND density ρ

$$\rho_{ij} = \epsilon_{ilm}\partial_l \beta^{\mathrm{e}}_{mj}, \tag{8}$$

$$= -\epsilon_{ilm}\partial_l \beta^{\mathrm{p}}_{mj}. \tag{9}$$

The elastic distortion field β^{e} is the sum of its symmetric strain and antisymmetric rotation fields,

$$\beta^{\mathrm{e}} = \epsilon^{\mathrm{e}} + \omega^{\mathrm{e}}, \tag{10}$$

where we assume linear elasticity, ignoring the 'geometric nonlinearity' in these tensors. Substituting the sum of two tensor fields into the incompatibility relation Eq. (8) gives

$$\rho_{ij} = \varepsilon_{ikl}\partial_k \omega^{\mathrm{e}}_{lj} + \varepsilon_{ikl}\partial_k \epsilon^{\mathrm{e}}_{lj}. \tag{11}$$

The elastic rotation tensor ω^{e} can be rewritten as an axial vector, the crystalline orientation vector Λ

$$\Lambda_k = \frac{1}{2}\varepsilon_{ijk}\omega^{\mathrm{e}}_{ij}, \tag{12}$$

or

$$\omega^{\mathrm{e}}_{ij} = \varepsilon_{ijk}\Lambda_k. \tag{13}$$

Thus we can substitute Eq. (13) into Eq. (11)

$$\rho_{ij} = (\delta_{ij}\partial_k \Lambda_k - \partial_j \Lambda_i) + \varepsilon_{ikl}\partial_k \epsilon^{\mathrm{e}}_{lj}. \tag{14}$$

For a system without residual elastic stress, the GND density thus depends only on the varying crystalline orientation (Limkumnerd and Sethna, 2007).

Dynamically, the time evolution law of the GND density emerges from the conservation of the Burgers vector (Kosevich, 1979; Lazar, 2011)

$$\frac{\partial}{\partial t} \rho_{ik} = -\varepsilon_{ijq} \partial_j J_{qk}, \tag{15}$$

or

$$\frac{\partial}{\partial t} \varrho_{ijk} = -\varepsilon_{ijm} \varepsilon_{mpq} \partial_p J_{qk} = -g_{ijpq} \partial_p J_{qk}, \tag{16}$$

where J represents the Burgers vector flux, and the symbol g_{ijpq} indicates $\varepsilon_{ijm}\varepsilon_{mpq} = \delta_{ip}\delta_{jq} - \delta_{iq}\delta_{jp}$.

2.1.2. Non-conserved order parameter field

The natural physicist's order parameter field ϱ, characterizing the incompatibility, can be written in terms of the plastic distortion field β^p

$$\varrho_{ijk} = \varepsilon_{ijm}\rho_{mk} = -g_{ijls}\partial_l\beta^p_{sk}. \tag{17}$$

In the linear approximation, the alternative order parameter field β^p fully specifies the local deformation $\boldsymbol{u}$ of the material, the elastic distortion β^e, the internal long-range stress field σ^{int} and the crystalline orientation (the Rodrigues vector $\boldsymbol{\Lambda}$ giving the axis and angle of rotation), as summarized in A.

It is natural, given Eqs. (9) and (15), to use the flux J of the Burgers vector density to define the dynamics of the plastic distortion tensor β^p (Kosevich, 1979; Limkumnerd and Sethna, 2006; Lazar, 2011):

$$\frac{\partial \beta^p_{ij}}{\partial t} = J_{ij}. \tag{18}$$

As noted by Acharya (2004), Eqs. (9) and (15) equate a curl of β^p to a curl of J, so an arbitrary divergence may be added to Eq. (18): the evolution of the plastic distortion β^p is not determined by the evolution of the GND density. Acharya (2004) resolves this ambiguity using a Stokes–Helmholtz decomposition of β^p. In our notation, $\beta^p = \beta^{p,I} + \beta^{p,H}$. The 'intrinsic' plastic distortion $\beta^{p,I}$ is divergence-free ($\partial_i\beta^{p,I}_{ij} = 0$, i.e., $k_i\widetilde{\beta}^{p,I}_{ij} = 0$), and determined by the GND density ρ. The 'history-dependent'[3] $\beta^{p,H}$ is curl-free ($\epsilon_{\ell ij}\partial_\ell\beta^{p,H}_{ij} = 0$, $\epsilon_{\ell ij}k_\ell\widetilde{\beta}^{p,H}_{ij} = 0$). In Fourier space, we can do this decomposition explicitly, as

$$\widetilde{\beta}^p_{ij}(\mathbf{k}) = -i\varepsilon_{ilm}\frac{k_l}{k^2}\widetilde{\rho}_{mj}(\mathbf{k}) + ik_i\widetilde{\psi}_j(\mathbf{k}) \equiv \widetilde{\beta}^{p,I}_{ij}(\mathbf{k}) + \widetilde{\beta}^{p,H}_{ij}(\mathbf{k}). \tag{19}$$

This decomposition will become important to us in Section 4.3.3, where the correlation functions of $\beta^{p,I}$ and $\beta^{p,H}$ will scale differently with distance.

Acharya (2004) treats the evolution of the two components $\beta^{p,I}$ and $\beta^{p,H}$ separately. Because our simulations have periodic boundary conditions, the evolution of $\beta^{p,H}$ does not affect the evolution of ρ. As noted by Acharya (2004), in more general situations $\beta^{p,H}$ will alter the shape of the body, and hence interact with the boundary conditions.[4] Hence in the simulations presented here, we use Eq. (18), with the warning that the plastic deformation fields shown in the figures are arbitrary up to an overall divergence. The correlation functions we study of the intrinsic plastic distortion $\beta^{p,I}$ are independent of this ambiguity, but the correlation functions of $\beta^{p,H}$ we discuss in the E.1 will depend on this choice.

In the presence of external loading, we can express the appropriate free energy $\mathcal{F}$ as the sum of two terms: the elastic interaction energy of GNDs, and the energy of interaction with the applied stress field. The free energy functional is

$$\mathcal{F} = \int d^3\mathbf{x}\left(\frac{1}{2}\sigma^{int}_{ij}\epsilon^e_{ij} - \sigma^{ext}_{ij}\epsilon^p_{ij}\right). \tag{20}$$

Alternatively, it can be rewritten in Fourier space

$$\mathcal{F} = -\int\frac{d^3\mathbf{k}}{(2\pi)^3}\left(\frac{1}{2}M_{ijmn}(\mathbf{k})\widetilde{\beta}^p_{ij}(\mathbf{k})\widetilde{\beta}^p_{mn}(-\mathbf{k}) + \widetilde{\sigma}^{ext}_{ij}(\mathbf{k})\widetilde{\beta}^p_{ij}(-\mathbf{k})\right), \tag{21}$$

as discussed in B.1.

---

[3] Changing the initial reference state through a curl-free plastic distortion (leaving behind no dislocations) will change $\beta^{p,H}$ but not $\beta^{p,I}$; the former depends on the history of the material and not just the current state, motivating our nomenclature.

[4] For our simulations with external shear (Chen et al., 2010), the $\mathbf{k} = 0$ of $\beta^{p,H}$ couples to the boundary condition. We determine the plastic evolution of the $\mathbf{k} = 0$ mode explicitly in that case. For correlation functions presented here, the $\mathbf{k} = 0$ mode is unimportant because we subtract β^p fields at different sites before correlating.

2.2. Traditional dissipative continuum dynamics

There are well known approaches for deriving continuum equations of motion for dissipative systems, which in this case produce a traditional von Mises-style theory (Rickman and Viñals, 1997), useful at longer scales. We begin by reproducing these standard equations.

For the sake of simplicity, we ignore external stress (σ_{ij} simplified to σ_{ij}^{int}) in the following three subsections. We start by using the standard methods applied to the non-conserved order parameter β^{p}, and then turn to the conserved order parameter ϱ.

2.2.1. Dissipative dynamics built from the non-conserved order parameter field β^{p}

The plastic distortion β^{p} is a non-conserved order parameter field, which is utilized by the engineering community to study texture evolution and plasticity of mechanically deformed structural materials. The simplest dissipative dynamics in terms of β^{p} minimizes the free energy by steepest descents

$$\frac{\partial}{\partial t}\beta_{ij}^{\text{p}} = -\Gamma \frac{\delta \mathcal{F}}{\delta \beta_{ij}^{\text{p}}}, \tag{22}$$

where Γ is a positive material-dependent constant. We may rewrite it in Fourier space, giving

$$\frac{\partial}{\partial t}\widetilde{\beta}_{ij}^{\text{p}}(\mathbf{k}) = -\Gamma \frac{\delta \mathcal{F}}{\delta \widetilde{\beta}_{ij}^{\text{p}}(-\mathbf{k})}. \tag{23}$$

The functional derivative $\delta \mathcal{F}/\delta \widetilde{\beta}_{ij}^{\text{p}}(-\mathbf{k})$ is the negative of the long-range stress

$$\frac{\delta \mathcal{F}}{\delta \widetilde{\beta}_{ij}^{\text{p}}(-\mathbf{k})} = -M_{ijmn}(\mathbf{k})\widetilde{\beta}_{mn}^{\text{p}}(\mathbf{k}) \equiv -\widetilde{\sigma}_{ij}(\mathbf{k}). \tag{24}$$

This dynamics implies a simplified version of von Mises plasticity

$$\frac{\partial}{\partial t}\widetilde{\beta}_{ij}^{\text{p}}(\mathbf{k}) = \Gamma \widetilde{\sigma}_{ij}(\mathbf{k}). \tag{25}$$

2.2.2. Dissipative dynamics built from the conserved order parameter field ϱ

We can also derive an equation of motion starting from the GND density ϱ, as was done by Rickman and Viñals (1997). For this dissipative dynamics Eq. (16), the simplest expression for J is

$$J_{qk} = -\Gamma'_{ablq}\partial_l \frac{\delta \mathcal{F}}{\delta \varrho_{abk}}, \tag{26}$$

where the material-dependent constant tensor Γ' must be chosen to guarantee a decrease of the free energy with time.

The infinitesimal change of $\mathcal{F}$ with respect to the GND density ϱ is

$$\delta \mathcal{F}[\varrho] = \int d^3\mathbf{x} \, \frac{\delta \mathcal{F}}{\delta \varrho_{ijk}} \delta \varrho_{ijk}. \tag{27}$$

The free energy dissipation rate is thus $\delta \mathcal{F}/\delta t$ for $\delta \varrho = \frac{\partial \varrho}{\partial t}\delta t$, hence

$$\frac{\partial}{\partial t}\mathcal{F}[\varrho] = \int d^3\mathbf{x} \, \frac{\delta \mathcal{F}}{\delta \varrho_{ijk}} \frac{\partial \varrho_{ijk}}{\partial t}. \tag{28}$$

Substituting Eq. (16) into Eq. (28) and integrating by parts gives

$$\frac{\partial}{\partial t}\mathcal{F}[\varrho] = \int d^3\mathbf{x} \left(g_{ijpq}\partial_p \frac{\delta \mathcal{F}}{\delta \varrho_{ijk}} \right) J_{qk}. \tag{29}$$

Substituting Eq. (26) into Eq. (29) gives

$$\frac{\partial}{\partial t}\mathcal{F}[\varrho] = -\int d^3\mathbf{x} \left(g_{ijpq}\partial_p \frac{\delta \mathcal{F}}{\delta \varrho_{ijk}} \right) \left(\Gamma'_{ablq}\partial_l \frac{\delta \mathcal{F}}{\delta \varrho_{abk}} \right). \tag{30}$$

Now, to guarantee that energy never increases, we choose $\Gamma'_{ablq} = \Gamma g_{ablq}$, ($\Gamma$ is a positive material-dependent constant), which yields the rate of change of energy as a negative of a perfect square

$$\frac{\partial}{\partial t}\mathcal{F}[\varrho] = -\int d^3\mathbf{x} \, \Gamma \sum_{q,k} \left(g_{ablq}\partial_l \frac{\delta \mathcal{F}}{\delta \varrho_{abk}} \right)^2. \tag{31}$$

Using Eqs. (16) and (26), we can write the dynamics in terms of ϱ

$$\frac{\partial}{\partial t}\varrho_{ijk} = \Gamma g_{ijpq}g_{ablq}\partial_p\partial_l\frac{\delta\mathcal{F}}{\delta\varrho_{abk}}.\tag{32}$$

Substituting the functional derivative $\delta\mathcal{F}/\delta\varrho_{abk}$, Eq. (B.10), derived in B.2, into Eq. (32) and comparing to Eq. (16) tells us

$$\frac{\partial}{\partial t}\varrho_{ijk}(\mathbf{x}) = -\Gamma g_{ijpq}\partial_p\sigma_{qk}(\mathbf{x}) = -g_{ijpq}\partial_p J_{qk}(\mathbf{x}),\tag{33}$$

where

$$J_{qk} = \Gamma\sigma_{qk}\tag{34}$$

duplicating the von Mises law (Eq. 25) of the previous subsection. The simplest dissipative dynamics of either non-conserved or conserved order parameter fields thus turns out to be the traditional linear dynamics, a simplified von Mises law.

The problem with this law for us is that it allows for plastic deformation in the absence of dislocations, i.e., the Burgers vector flux can be induced through the elastic loading on the boundaries, even in a defect-free medium. This is appropriate on engineering length scales above or around a micron, where SSDs dominate the plastic deformation. (Methods to incorporate their effects into a theory like ours have been provided by Acharya and Roy (2006), Roy and Acharya (2006) and Varadhan et al. (2006)).

By ignoring the SSDs, our theory assumes that there is an intermediate coarse-grain length scale, large compared to the distance between dislocations and small compared to the distance where the cancellation of dislocations with different Burgers vectors dominates the dynamics, discussed in Section 3. We believe this latter length scale is given by the distance between cell walls (as discussed in Section 4.2). The cell wall misorientations are geometrically necessary. On the one hand, it is known (Kuhlmann-Wilsdorf and Hansen, 1991; Hughes and Hansen, 1993) that neighboring cell walls often have misorientations of alternating signs, so that on coarse-grain length scales just above the cell wall separation one would expect explicit treatment of the SSDs would be necessary. On the other hand, the density of dislocations in cell walls is high, so that a coarse-grain length much smaller than the interesting structures (and hence where we believe SSDs are unimportant) should be possible (Kiener et al., 2011). (Our cell structures are fractal, with no characteristic 'cell size'; this coarse-grain length sets the minimum cutoff scale of the fractal, and the grain size or inhomogeneity length will set the maximum scale.) With this assumption, to treat the formation of cellular structures, we turn to theories of the form given in Eq. (15), defined in terms of dislocation currents J that depend directly on the local GND density.

2.3. Our CDD model

The microscopic motion of a dislocation under external strain depends upon temperature. In general, it moves quickly along the glide direction, and slowly (or not at all) along the climb direction where vacancy diffusion must carry away the atoms. The glide speed can be limited by phonon drag at higher temperatures, or can accelerate to nearly the speed of sound at low temperatures (Hirth and Lothe, 1982). It is traditional to assume that the dislocation velocity is over-damped, and proportional to the component of the force per unit dislocation length in the glide plane.[5]

To coarse-grain this microscopics, for reasons described in Section 3, we choose a CDD model whose dislocation currents vanish when the GND density vanishes, without considering SSDs. Limkumnerd and Sethna (2006) derived a dislocation current J for this case using a closure approximation of the underlying microscopics. Their work reproduced (in the case of both glide and climb) an earlier dynamical model proposed by Acharya et al. (Acharya, 2001; Roy and Acharya, 2005; Acharya and Roy, 2006), who also incorporate the effects of SSDs. We follow the general approach of Acharya and collaborators (Acharya, 2001, 2003, 2004; Roy and Acharya, 2005; Varadhan et al., 2006; Acharya and Roy, 2006) in Section 2.3.1 to derive an evolution law for dislocations allowed both to glide and climb, and then modify it to remove climb in Section 2.3.2. We derive a second variant of glide-only dynamics in Section 2.3.3 by coupling climb to vacancies and then taking the limit of infinite vacancy energy, which reproduces a model proposed earlier by Acharya and Roy (2006).

In our CGD and GOD-LVP dynamics (Sections 2.3.1 and 2.3.3 below), all dislocations in the infinitesimal volume at $\mathbf{x}$ are moving with a common velocity $\boldsymbol{v}(\mathbf{x})$. We discuss the validity of this single-velocity form for the equations of motion at length in Section 3, together with a discussion of the coarse-graining and the emergence of SSDs. We view our simulations as physically sensible 'model materials' – perhaps not the correct theory for any particular material, but a sensible framework to generate theories of plastic deformation and explain generic features common to many materials.

2.3.1. Climb-glide dynamics (CGD)
We start with a model presuming (perhaps unphysically) that vacancy diffusion is so fast that dislocations climb and glide with equal mobility. The elastic Peach–Koehler force due to the stress $\sigma(\mathbf{x})$ on the local GND density is given by $f_u^{PK} = \sigma_{mk}\varrho_{umk}$. We assume that the velocity $\boldsymbol{v} \propto \boldsymbol{f}^{PK}$, giving a local constitutive relation

$$v_u \propto \sigma_{mk}\varrho_{umk}.\tag{35}$$

---

[5] In real materials the dislocation dynamics is intermittent, as dislocations bow out or depin from junctions and disorder, and engage in complex dislocation avalanches.

How should we determine the proportionality constant between velocity and force? In experimental systems, this is complicated by dislocation entanglement and short-range forces between dislocations. Ignoring these features, the velocity of each dislocation should depend only on the stress induced by the other dislocations, not the local density of dislocations (Zapperi and Zaiser, 2011). We can incorporate this in an approximate way by making the proportionality factor in Eq. (35) inversely proportional to the GND density. We measure the latter by summing the square of all components of ϱ, hence $|\varrho| = \sqrt{\varrho_{ijk}\varrho_{ijk}/2}$ and $v_u = \frac{D}{|\varrho|}\sigma_{mk}\varrho_{umk}$, where D is a positive material-dependent constant. This choice has the additional important feature that the evolution of a sharp domain wall whose width is limited by the lattice cutoff is unchanged when the lattice cutoff is reduced.

The flux J of the Burgers vector is thus (Kosevich, 1979)

$$J_{ij} = v_u \varrho_{uij} = \frac{D}{|\varrho|}\sigma_{mk}\varrho_{umk}\varrho_{uij}. \tag{36}$$

Notice that this dynamics satisfies our criterion that $J = 0$ when there are no GNDs (i.e., $\varrho = 0$). Notice also that we do not incorporate the effects of SSDs (Acharya's L^p (Acharya and Roy, 2006)); we discuss this further in Section 3.

Substituting this flux J (Eq. (36)) into the free energy dissipation rate (Eq. (B.16)) gives

$$\frac{\partial \mathcal{F}}{\partial t} = -\int d^3\mathbf{x}\,\sigma_{ij}J_{ij} = -\int d^3\mathbf{x}\,\frac{|\varrho|}{D}v^2 \leqslant 0. \tag{37}$$

Details are given in B.3.

2.3.2. Glide-only dynamics: mobile dislocation population (GOD-MDP)

When the temperature is low enough, dislocation climb is negligible, i.e., dislocations can only move in their glide planes. Fundamentally, dislocation glide conserves the total number of atoms, which leads to an unchanged local volume. Since the local volume change in time is represented by the trace J_{ii} of the flux of the Burgers vector, conservative motion of GNDs demands $J_{ii} = 0$. Limkumnerd and Sethna (2006) derived the equation of motion for dislocation glide only, by removing the trace of J from Eq. (36). However, their dynamics fails to guarantee that the free energy monotonically decreases. Here we present an alternative approach.

We can remove the trace of J by modifying the first equality in Eq. (36),

$$J'_{ij} = v'_u\left(\varrho_{uij} - \frac{1}{3}\delta_{ij}\varrho_{ukk}\right), \tag{38}$$

where $\varrho'_{uij} = \varrho_{uij} - \frac{1}{3}\delta_{ij}\varrho_{ukk}$ can be viewed as a subset of 'mobile' dislocations moving with velocity $\boldsymbol{v}'$.

Substituting the current (Eq. (38)) into the free energy dissipation rate (Eq. (B.16)) gives

$$\frac{\partial \mathcal{F}}{\partial t} = -\int d^3\mathbf{x}\,\sigma_{ij}\left(v'_u\varrho'_{uij}\right). \tag{39}$$

If we choose the velocity $v'_u \propto \sigma_{ij}\varrho'_{uij}$, the appropriate free energy monotonically decreases in time. We thus express $v'_u = \frac{D}{|\varrho|}\varrho'_{uij}\sigma_{ij}$, where D is a positive material-dependent constant, and the prefactor $1/|\varrho|$ is added for the same reasons, as discussed in the second paragraph of Section 2.3.1.

The current J' of the Burgers vector is thus written (Chen et al., 2010)

$$J'_{ij} = v'_u\varrho'_{uij} = \frac{D}{|\varrho|}\sigma_{mn}\left(\varrho_{umn} - \frac{1}{3}\delta_{mn}\varrho_{ull}\right)\left(\varrho_{uij} - \frac{1}{3}\delta_{ij}\varrho_{ukk}\right). \tag{40}$$

This natural evolution law becomes much less self-evident when expressed in terms of the traditional two-index version ρ (Eqs. (1) and (2))

$$J'_{ij} = \frac{D}{|\varrho|}\left(\sigma_{in}\rho_{mn}\rho_{mj} - \sigma_{mn}\rho_{in}\rho_{mj} - \frac{1}{3}\sigma_{mm}\rho_{ni}\rho_{nj} + \frac{1}{3}\sigma_{mm}\rho_{in}\rho_{nj} - \frac{\delta_{ij}}{3}\left(\sigma_{kn}\rho_{mn}\rho_{mk} - \sigma_{mn}\rho_{kn}\rho_{mk} - \frac{1}{3}\sigma_{mm}\rho_{nk}\rho_{nk} + \frac{1}{3}\sigma_{mm}\rho_{kn}\rho_{nk}\right)\right), \tag{41}$$

(which is why we introduce the three-index variant ϱ).

This current J' makes the free energy dissipation rate the negative of a perfect square in Eq. (B.18). Details are given in B.3.

2.3.3. Glide-only dynamics: local vacancy-induced pressure (GOD-LVP)

At high temperature, the fast vacancy diffusion leads to dislocation climb out of the glide direction. As the temperature decreases, vacancies are frozen out so that dislocations only slip in the glide planes. In C.1, we present a dynamical model coupling the vacancy diffusion to our CDD model. Here we consider the limit of frozen-out vacancies with infinite energy costs, which leads to another version of glide-only dynamics.
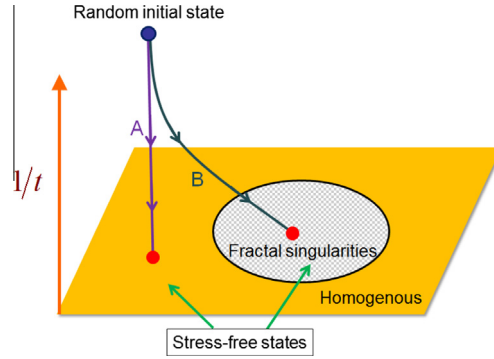
Fig. 3. Relaxation of various CDD models. The blue dot represents the initial random plastically-deformed state; the red dots indicate the equilibrated stress-free states driven by different dynamics. Curve A: steepest decent dynamics leads to the trivial homogeneous equilibrated state, discussed in Section 2.2. Curve B: our CDD models settle the system into non-trivial stress-free states with wall-like singularities of the GND density, discussed in Section 2.3. (For interpretation of the references to color in this figure legend, the reader is referred to the web version of this article.)

According to the coupling dynamics Eq. (C.8), we write down the general form of dislocation current

$$J''_{ij} = \frac{D}{|\varrho|}(\sigma_{mn} - \delta_{mn}p)\varrho_{umn}\varrho_{uij}, \tag{42}$$

where p is the local pressure due to vacancies.

The limit of infinitely costly vacancies ($\alpha \to \infty$ in C.1) leads to the traceless current, $J''_{ii} = 0$. Solving this equation gives a critical local pressure p^c

$$p^c = \frac{\sigma_{pq}\varrho_{spq}\varrho_{skk}}{\varrho_{uaa}\varrho_{ubb}}. \tag{43}$$

The corresponding current J'' of the Burgers vector in this limit is thus written

$$J''_{ij} = \frac{D}{|\varrho|}\left(\sigma_{mn} - \frac{\sigma_{pq}\varrho_{spq}\varrho_{skk}}{\varrho_{uaa}\varrho_{ubb}}\delta_{mn}\right)\varrho_{umn}\varrho_{uij}, \tag{44}$$

reproducing the glide-only dynamics proposed by Acharya and Roy (2006).

Substituting the current (Eq. (44)) into the free energy dissipation rate (Eq. (B.16)) gives

$$\frac{\partial \mathcal{F}}{\partial t} = -\int d^3\mathbf{x}\frac{D}{|\varrho|}\left[f_i^{PK}f_i^{PK} - \left(\frac{d_i f_i^{PK}}{|\mathbf{d}|}\right)^2\right] \leqslant 0, \tag{45}$$

where $f_i^{PK} = \sigma_{mn}\varrho_{imn}$ and $d_i = \varrho_{ikk}$. The equality emerges when the force $\mathbf{f}^{PK}$ is along the same direction as $\mathbf{d}$.

Unlike the traditional linear dissipative models, our CDD model, coarse grained from microscopic interactions, drives the random plastic distortion to non-trivial stress-free states with dislocation wall singularities, as schematically illustrated in Fig. 3.

Our minimal CDD model, consisting of GNDs evolving under the long-range interaction, provides a framework for understanding dislocation morphologies at the mesoscale. Eventually, it can be extended to include vacancies by coupling them to the dislocation current (as discussed in C.1, or extended to include disorder, dislocation pinning, and entanglement by adding appropriate interactions to the free energy functional and refining the effective stress field (as discussed in C.2). It has already been extended to include SSDs incorporating traditional crystal plasticity theories (Varadhan et al., 2006; Acharya and Roy, 2006; Roy and Acharya, 2006).

3. Coarse graining

The discussion in Section 2 uses the language and conceptual framework of the condensed matter physics of systems close to equilibrium – the generalized "hydrodynamics" used to derive equations of motion for liquids and gases, liquid crystals, superfluids and superconductors, magnetic materials, etc. In these subjects, one takes the broken symmetries and conserved quantities, and systematically writes the most general evolution laws allowed by symmetry, *presuming that these quantities determine the state of the material*. In that framework, the Burgers vector flux J of Eqs. (15) and (16) would normally be written as a general function of ρ and its gradients, constrained by symmetries and the necessity that the net energy decreases with time. Indeed, this was the approach Limkumnerd originally took (Limkumnerd, 2006), but the complexity of the resulting theory and the multiplicity of terms allowed by symmetry led them to specialize (Limkumnerd and Sethna, 2006)

to a particular choice motivated by the Peach–Koehler force – leading to the equation of motion previously developed by Acharya (2001) and Roy and Acharya (2005).

The assumption that the net continuum dislocation density determines the evolution, however, is an uncontrolled[6] and probably invalid assumption. Falk and Langer (1998) have argued that the chaotic motion of dislocations may lead to a statistical ensemble that could allow a systematic theory of this type to be justified, but consensus has not been reached on whether this will indeed be possible.) The situation is less analogous to deriving the Navier–Stokes equation (where local equilibrium at the viscous length is sensible) than to deriving theories of eddy viscosity in fully developed turbulence (where unavoidable uncontrolled approximations are needed to subsume swirls on smaller scales into an effective viscosity of the coarse-grained system). Important features of how dislocations are arranged in a local region will not be determined by the net Burgers vector density, and extra state variables embodying their effects are needed. In the context of dislocation dynamics, these state variables are usually added as SSDs and yield surfaces – although far more complex memory effects could in principle be envisioned.

Let us write ρ^0 as the microscopic dislocation density (the sum of line-δ functions along individual dislocations, as in Eq. (1) and following equations). For the microscopic density, allowing both glide and climb, the dislocation current J^0 is directly given by the velocity $\boldsymbol{v}^0(\mathbf{x})$ of the individual dislocation passing through $\mathbf{x}$ (see Eq. (36)):

$$J_{ij}^0 = v_u^0 \varrho_{uij}^0. \tag{46}$$

Let F^σ be the microscopic quantity F^0 coarse-grained density over a length-scale Σ,

$$F_{ij}^\Sigma(\mathbf{x}) = \int d^3\mathbf{y} F_{ij}^0(\mathbf{x}+\mathbf{y}) w^\Sigma(\mathbf{y}), \tag{47}$$

where w^Σ is a smoothing or blurring function. Typically, we use a normal or Gaussian distribution N^Σ

$$w^\Sigma(\mathbf{y}) = N^\Sigma(\mathbf{y}) = (2\pi\Sigma^2)^{-3/2} e^{-y^2/(2\Sigma^2)}. \tag{48}$$

For our purposes, we can *define* the SSD density as the difference between the coarse-grained density and the microscopic density (Sandfeld et al., 2010):

$$\rho^{SSD}(\mathbf{x}) = \rho^0(\mathbf{x}) - \rho^\Sigma(\mathbf{x}) = \rho^0(\mathbf{x}) - \int d^3\mathbf{y}\rho^0(\mathbf{x}+\mathbf{y})w^\Sigma(\mathbf{y}). \tag{49}$$

(Acharya (2011) calls this quantity the dislocation fluctuation tensor field.)

First, we address the question of SSDs, which we do not include in our simulations. In the past (Chen et al., 2010), we have argued that they do not contribute to the long-range stresses that drive the formation of the cell walls, and that the successful generation of cellular structures in our simplified model suggests that they are not crucial. Here we go further, and suggest that their density may be small on the relevant length-scales for cell-wall formation, and also that in a theory (like ours) with scale-invariant structures it would not be consistent to add them separately.

What is the dependence of the SSD density on the coarse-graining scale? Clearly ρ^0 contains all dislocations; clearly for a bent single crystal of size L, ρ^L contains only those dislocations necessary to mediate the rotation across the crystal (usually a tiny fraction of the total density of dislocations). As Σ increases past the distance between dislocations, canceling pairs of Burgers vectors through the same grid face will leave the GNDs and join the SSDs. If the dislocation densities were smoothly varying, as is often envisioned on long length scales, the SSD density would be roughly independent of Σ except on microscopic scales. But, for a cellular structure with gross inhomogeneities in dislocation density, the SSD density on the mesoscale may be much lower than that on the macroscale. Very tangibly, if alternating cell walls separated by ℓ have opposite misorientations (as is quite commonly observed (Kuhlmann-Wilsdorf and Hansen, 1991; Hughes and Hansen, 1993)), then the SSD density for $\Sigma > \ell$ will include most of the dislocations incorporated into these cell walls, while for $\Sigma < \ell$ the cell walls will be viewed as geometrically necessary.

How does the GND density within the cell walls compare with the total dislocation density for a typical material? Is it possible that the GNDs dominate over SSDs in the regime where these cell wall patterns form? Recent simulations clearly suggest (see Kiener et al., 2011, Figure. 5) that the distinction between GNDs and SSDs is not clear at the length scale of a micron, and with reasonable definitions GNDs dominate by at least an order of magnitude over the residual average SSD density. But what about the experiments? While more experiments are necessary to clarify this issue, the existing evidence supports that at mesoscales, SSDs at least are not necessarily dominant. In particular, Hughes et al. (1997) observes that cell boundary structures exhibit $D_{av}\theta_{av}/b = C$ where D_{av} is the average wall spacing and θ_{av} is the average misorientation angle with $C \sim 650$ for 'geometrically necessary' boundaries (GNBs) and $C \sim 80$ for 'incidental dislocation' boundaries (IDBs). The resulting dislocation density should scale as

$$\rho_{GND} = \frac{1}{D_{av}h} = \frac{\theta_{av}}{D_{av}b} \sim \frac{C}{D_{av}^2} = \frac{\theta_{av}^2}{b^2 C}, \tag{50}$$

---

[6] There are two uncontrolled approximations we make. Here we assume that the continuum, coarse-grained dislocation density $\rho = \rho^\Sigma$ determines the evolution: we ignore SSDs as unimportant on the sub-cellular length-scales of interest to us. Later, we shall further assume that the nine independent components of ρ_{ij} all are dragged by the stress with the same velocity.

where h is the average spacing between GNDs in the wall.[7] There are some estimates available from the literature. Hughes et al. (1997) tells us for pure aluminum that D_{av} is often observed to be $D_{av} = 1 - 5$ μm which leads to roughly $\rho_{GND}^{GNB} \sim 10^{13}$ $\times (2.6 - 65)/\text{m}^2$ and ρ_{GND}^{IDB} one order of magnitude smaller. Similar estimates in Godfrey and Hughes (2000) give $\rho_{GND}^{GNB} = 10^{14} - 6 \times 10^{15}/\text{m}^2$ for aluminum at von Mises strains of $\epsilon = 0.2$ and 0.6, respectively. The larger von Mises strains, the higher dislocation density. Typically, in highly deformed aluminum ($\epsilon \sim 2.7$), the total dislocation density is roughly $10^{16}/\text{m}^2$ (see Hughes et al., 1998). While SSDs within a cell boundary may exist, it is clearly far from true that SSDs dominate the dynamics in these experiments.

These TEM analyses of cell boundary sizes and misorientations have a misorientation cutoff $\theta_0 \sim 2°$ (Liu, 1994); they analyze the cell boundaries using a single typical length scale D_{av}. Our model behavior is formally much closer to the fractal scaling analysis that Hähner et al. (1998) used. How does one identify a cutoff in a theory exhibiting scale invariance (i.e., with no natural length scale)? Clearly our simulations are cut off at the numerical grid spacing, and the scale invariant theory applies after a few grid spacings. Similarly, if the real materials are described by a scale-invariant morphology (still an open question), the cutoff to the scale invariant regime will be where the granularity of the dislocations becomes important – the dislocation spacing, or perhaps the annihilation length. This is precisely the length scale at which the dislocations are individually resolved – at which there is no separate populations of SSDs and GNDs. Thus ignoring SSDs in our theory is at least self-consistent.

So, not only are the SSDs unimportant for the long-range stresses and appear unnecessary for our (presumably successful) modeling of the formation of cell walls, but they also may be rare on the sub-cellular coarse-graining scale we use in our modeling, and it makes sense in our mesoscale theory for us to omit their effects.

The likelihood that we do not need to incorporate explicit SSDs in our equations of motion does not mean that our equations are correct. The microscopic equation of motion, Eq. (46) naively looks the same as our 'single-velocity' equation of motion we use (e.g., Eq. (36)). But, as derived in Acharya and Roy (2006), the coarse-graining procedure (Eq. (47)) leads to a correction term L^p to the single-velocity equations:

$$J_{ij}^{\Sigma} = (v_s^0 \varrho_{sij}^0)^{\Sigma} = v_s^{\Sigma} \varrho_{sij}^{\Sigma} + \left[(v_s^0 \varrho_{sij}^0)^{\Sigma} - v_s^{\Sigma} \varrho_{sij}^{\Sigma} \right] = v_s^{\Sigma} \varrho_{sij}^{\Sigma} + L_{ij}^p. \tag{51}$$

Acharya interprets[8] this correction term L^p as the strain rate due to SSDs (Acharya and Roy, 2006; Roy and Acharya, 2006), and later Beaudoin (Varadhan et al., 2006) and others (Mach et al., 2010) then use traditional crystal plasticity SSD evolution laws for it. Their GNDs thus move according to the same single-velocity laws as ours do, supplemented by SSDs that evolve by crystal plasticity (and thereby contribute changes to the GND density). This is entirely appropriate for scales large compared to the cellular structures, where most of the dislocations are indeed SSDs.

Although we argue that SSDs are largely absent at the nanoscale where we are using our continuum theory, this does not mean the single-velocity form of our equations of motion can be trusted. Unlike fluid mixtures, where momentum conservation and Galilean invariance lead to a shared mean velocity after a few collision times, the microscopic dislocations are subject to different resolved shear stresses and are mobile along different glide planes, so neighboring dislocations may well move in a variety of directions (Sandfeld et al., 2010). If so, the microscopic velocity $\boldsymbol{v^0}$ will fluctuate in concert with the microscopic Burgers vector density ϱ^0 on microscopic scales, and the correction L^p will be large. Hence Acharya's correction term L^p also incorporates multiple velocities for the GND density. Our single-velocity approximation (e.g., Eq. (36)) must be viewed as a physically allowed equation of motion, but a second uncontrolled approximation – the general evolution law for the coarse-grained system will be more complex.

Let us be perfectly clear that our arguments, compelling on scales small compared to the mesoscale cellular structures, should not be viewed as a critique of the use of SSDs on larger scales. Much of our understanding of yield stress and work hardening revolves around the macroscopic dislocation density, which perforce are due to SSDs (since they dominate on macroscopic scales). We also admire the work of Beaudoin, Acharya, and others which supplements the GND equations we both study with crystal plasticity rules for the SSDs motivated by Eq. (51). Surely on macroscales the SSDs dominate the deformation, and using a single-velocity law for the GNDs is better than ignoring them altogether, and we have no particular reason to believe that the contribution of multiple GND velocities in the evolution laws through L^p will be significant or dominant.

## 4. Results

4.1. Two and three dimensional simulations

We perform simulations in 2D and 3D for the dislocation dynamics of Eqs. (15) and (18), with dynamical currents defined by CGD (Eq. (36)), GOD-MDP (Eq. (40)), and GOD-LVP (Eq. (44)). We numerically observe that simulations of Eqs. (15) and

---

[7] Only misorientation mediating dislocations are counted.

[8] More precisely, Eq. (4) of Acharya and Roy (2006) contains two different definitions for L^p; the one in Eq. (51) and $L_{ij}^{p'} = \left[(v_s^0 (\varrho_{sij}^0 - \varrho_{sij}^{\Sigma}))^{\Sigma} \right] = \left[(v_s^0 \varrho_{sij}^{SSD})^{\Sigma} \right]$. $L^{p'}$ is of course a strain rate due to SSDs, but since ϱ^{Σ} varies in space $L^{p'}$ is not equal to L^p. Acharya (2012) suggests using a two-variable version of the SSD density, $\tilde{\varrho}^{SSD}(\mathbf{x}, \mathbf{x}') = \varrho^0(\mathbf{x}') - \varrho^{\Sigma}(\mathbf{x})$, making the two definitions equivalent.

(18) lead to the same results statistically (i.e., the numerical time step approximations leave the physics invariant). We therefore focus our presentation on the results of Eq. (18), where the evolving field variable β^p is unconstrained. Our CGD and GOD-MDP models have been quite extensively simulated in one and two dimensions and relevant results can be found in Limkumnerd and Sethna (2006), Limkumnerd and Sethna (2008) and Chen et al. (2010). In this paper, we concentrate on periodic grids of spatial extent L in both two (Chen et al., 2010) and three dimensions. The numerical approach we use is a second-order central upwind scheme designed for Hamilton–Jacobi equations (Kurganov et al., 2001) using finite differences. This method is quite efficient in capturing δ-shock singular structures (Choi et al., 2012b), even though it is flexible enough to allow for the use of approximate solvers near the singularities.

Our numerical simulations show a close analogy to those of turbulent flows (Choi et al., 2012b). As in three-dimensional turbulence, defect structures lead to intermittent transfer of morphology to short length scales. As conjectured (Pumir and Siggia, 1992a; Pumir and Siggia, 1992b) for the Euler equations or the inviscid limit of Navier–Stokes equations, our simulations develop singularities in finite time (Limkumnerd and Sethna, 2006; Chen et al., 2010). Here these singularities are δ-shocks representing grain-boundary-like structures emerging from the mutual interactions among mobile dislocations (Choi et al., in preparation). In analogy with turbulence, where the viscosity serves to smooth out the vortex-stretching singularities of the Euler equations, we have explored the effects of adding an artificial viscosity term to our equations of motion (Choi et al., 2012b). In the presence of artificial viscosity, our simulations exhibit nice numerical convergence in all
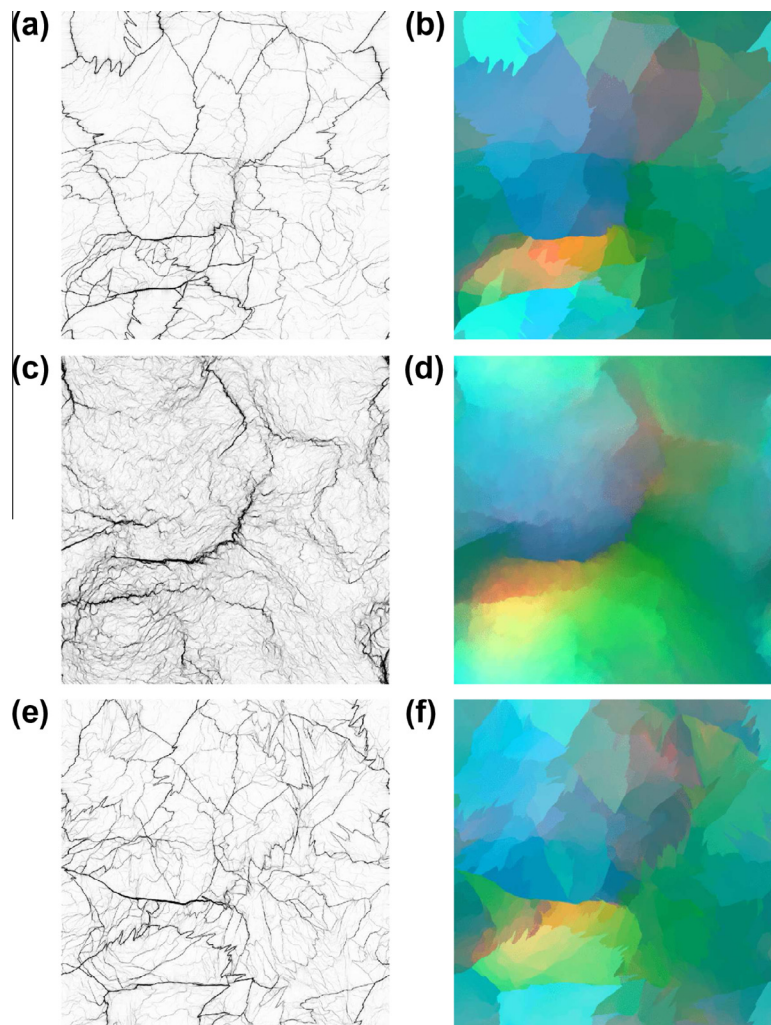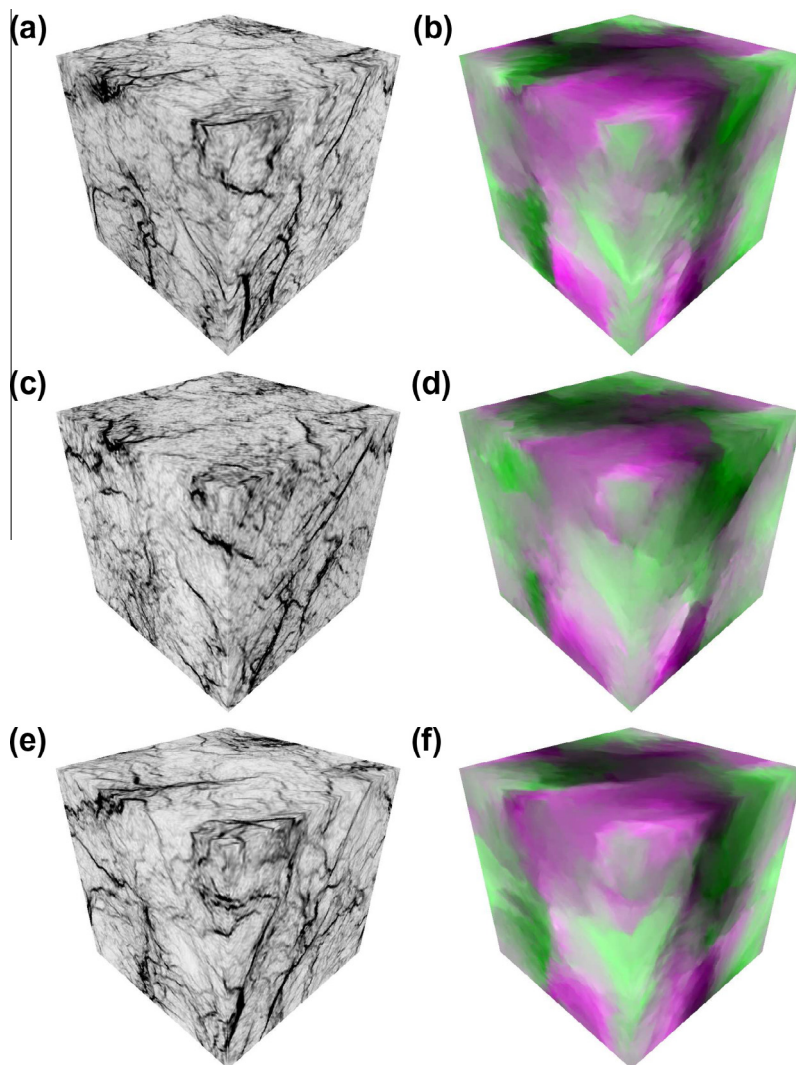

Fig. 4. Complex dislocation structures in two dimensions (1024^2) for the relaxed states of an initially random distortion. *Top:* Dislocation climb is allowed; *Middle:* Glide only using a mobile dislocation population; *Bottom:* Glide only using a local vacancy pressure. *Left:* Net GND density $|\varrho|$ plotted linearly in density with dark regions a factor $\sim 10^4$ more dense than the lightest visible regions. (a) When climb is allowed, the resulting morphologies are sharp, regular, and close to the system scale. (c) When climb is forbidden using a mobile dislocation population, there is a hierarchy of walls on a variety of length scales, getting weaker on finer length scales. (e) When climb is removed using a local vacancy pressure, the resulting morphologies are as sharp as those (a) allowing climb. *Right:* Corresponding local crystalline orientation maps, with the three components of the orientation vector Λ linearly mapped onto a vector of RGB values. Notice the fuzzier cell walls (c) and (d) suggests a larger fractal dimension.

dimensions (Choi et al., in preparation). However, in the limit of vanishing viscosity, the solutions of our dynamics continue to depend on the lattice cutoff in higher dimensions, (our simulations only exhibit numerical convergence in one dimension). Actually, the fact that the physical system is cut off by the atomic scale leads to the conjecture that our equations are in some sense non-renormalizable in the ultraviolet. These issues are discussed in detail in Choi et al. (in preparation) and Choi et al. (2012b)). See also Acharya and Tartar (2011) for global existence and uniqueness results from an alternative regularization for this type of equations; it is not known whether these alternative regularizations will continue to exhibit the fractal scaling we observe.

In the vanishing viscosity limit, our simulations exhibit fractal structure down to the smallest scales. When varying the system size continuously, the solutions of our dynamics exhibit a convergent set of correlation functions of the various order parameter fields, which are used to characterize the emergent self-similarity. This statistical convergence is numerically tested in D.1.

In both two and three dimensional simulations, we relax the deformed system with and without dislocation climb in the absence of external loading. Here, the initial plastic distortion field β^p is still a Gaussian random field with correlation length scale $\sqrt{2}L/5 \sim 0.28L$ and initial amplitude $\beta_0 = 1$. (In our earlier work (Chen et al., 2010), we described this length as $L/5$, using a non-standard definition of correlation length scale; see D.2.) These random initial conditions are explained in D.2. In 2D, Fig. 4 shows that CGD and GOD-LVP simulations (top and bottom) exhibit much sharper, flatter boundaries than GOD-MDP (middle). This difference is quantitatively described by the large shift in the static critical exponent η in 2D for

Fig. 5. Complex dislocation structures in three dimensions (128^3) for the relaxed states of an initially random distortion. Notice these textured views on the surface of simulation cubes. *Top:* Dislocation climb is allowed; *Middle:* Glide only using a mobile dislocation population; *Bottom:* Glide only using a local vacancy pressure. *Left:* Net GND density $|\varrho|$ plotted linearly in density with dark regions a factor $\sim 10^3$ more dense than the lightest visible regions. The cellular structures in (a), (c), and (e) seem similarly fuzzy; our theory in three dimensions generates fractal cell walls. *Right:* Corresponding local crystalline maps, with the three components of the orientation vector Λ linearly mapped onto a vector of RGB values.
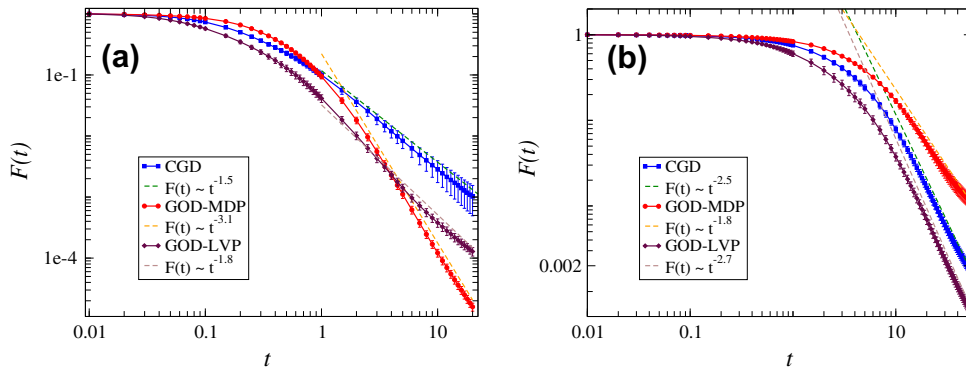
Fig. 6. The elastic free energy decreases to zero as a power law in time in both two and three dimensions. In both (a) and (b), we show that the free energy $\mathcal{F}$ decays monotonically in time, and goes to zero as a power law for CGD, GOD-MDP, and GOD-LVP simulations, as the system relaxes in the absence of external strain.

both CGD and GOD-LVP. In our earlier work (Chen et al., 2010), we announced this difference as providing a sharp distinction between high-temperature, non-fractal grain boundaries (for CGD), and low-temperature, fractal cell wall structures (for GOD-MDP). This appealing message did not survive the transition to 3D; Fig. 5 shows basically indistinguishable complex cellular structures, for all three types of dynamics. Indeed, Table 1 shows only a small change in critical exponents, among CGD, GOD-MDP, and GOD-LVP. During both two and three dimensional relaxations, their appropriate free energies monotonically decay to zero as shown in Fig. 6.

4.2. Self-similarity and initial conditions

Self-similar structures, as emergent collective phenomena, have been studied in mesoscale crystals (Chen et al., 2010), human-scale social network (Song et al., 2005), and the astronomical-scale universe (Vergassola et al., 1994). In some models (Vergassola et al., 1994), the self-similarity comes from *scale-free* initial conditions with a power-law spectrum (Peebles, 1993; Coles and Lucchin, 1995). In our CDD model, our simulations start from a random plastic distortion with a Gaussian distribution characterized by a single length scale. The scale-free dislocation structure spontaneously emerges as a result of the deterministic dynamics.

Our Gaussian random initial condition is analogous to hitting a bulk material randomly with a hammer. The hammer head (the dent size scale) corresponds to the correlated length. We need to generate inhomogeneous deformations like random dents, because our theory is deterministic and hence uniform initial conditions under uniform loading will not develop patterns.

We have considered alternatives to our imposition of Gaussian random deformation fields as initial conditions. (a) As an alternative to random initial deformations, we could have imposed a more regular (albeit nonuniform) deformation – starting with our material bent into a sinusoidal arc, and then letting it relax. Such simulations produce more symmetric versions of the fractal patterns we see; indeed, our Gaussian random initial deformations have correlation lengths 'hammer size' comparable to the system size, so our starting deformations are almost sinusoidal (although different components have different phases) – see D.2. (b) To explore the effects of multiple uncorrelated random domains (multiple small dents), we reduce the Gaussian correlation length as shown in Fig. 7. We find that the initial-scale deformation determines the maximal cutoff for the fractal correlations in our model. In other systems (such as two-dimensional turbulence) one can observe an 'inverse cascade' with fractal structures propagating to long length scales; we observe no evidence of these here. (c) As an alternative to imposing an initial plastic deformation field and then relaxing, we have explored deforming the material slowly and continuously in time. Our preliminary 'slow hammering' explorations turn the Gaussian initial conditions β^{p0} into a source term, modifying Eq. (18) with an additional term to give $\partial_t \beta_{ij}^p = J_{ij} + \beta_{ij}^{p0}/\tau$. Our early explorations suggest that slow hammering simulations will be qualitatively compatible with the relaxation of an initial rapid hammering. In this paper, to avoid the introduction of the hammering time scale τ, we focus on the (admittedly less physically motivated) relaxation behavior.

In real materials, initial grain boundaries, impurities, or sample sizes, can be viewed as analogies to our initial dents – explaining the observation of dislocation cellular structures both in single crystals and polycrystalline materials.

Fig. 7 shows relaxation without dislocation climb (due to the constraint of a mobile dislocation population) at various initial length scales in 2D. From Fig. 7(a) to (f), the net GND density, the net plastic distortion, and the crystalline orientation map, measured at two well-relaxed states evolved from different random distortions, all show fuzzy fractal structures, distinguished only by their longest-length-scale features that originate from the initial conditions. In Fig. 7(g)–(i), the correlation functions of the GND density ρ, the intrinsic plastic distortion $\beta^{p,I}$, and the crystalline orientation Λ are applied to characterize the emergent self-similarity, as discussed in the following Section 4.3. They all exhibit the same power law, albeit with different cutoffs due to the initial conditions.
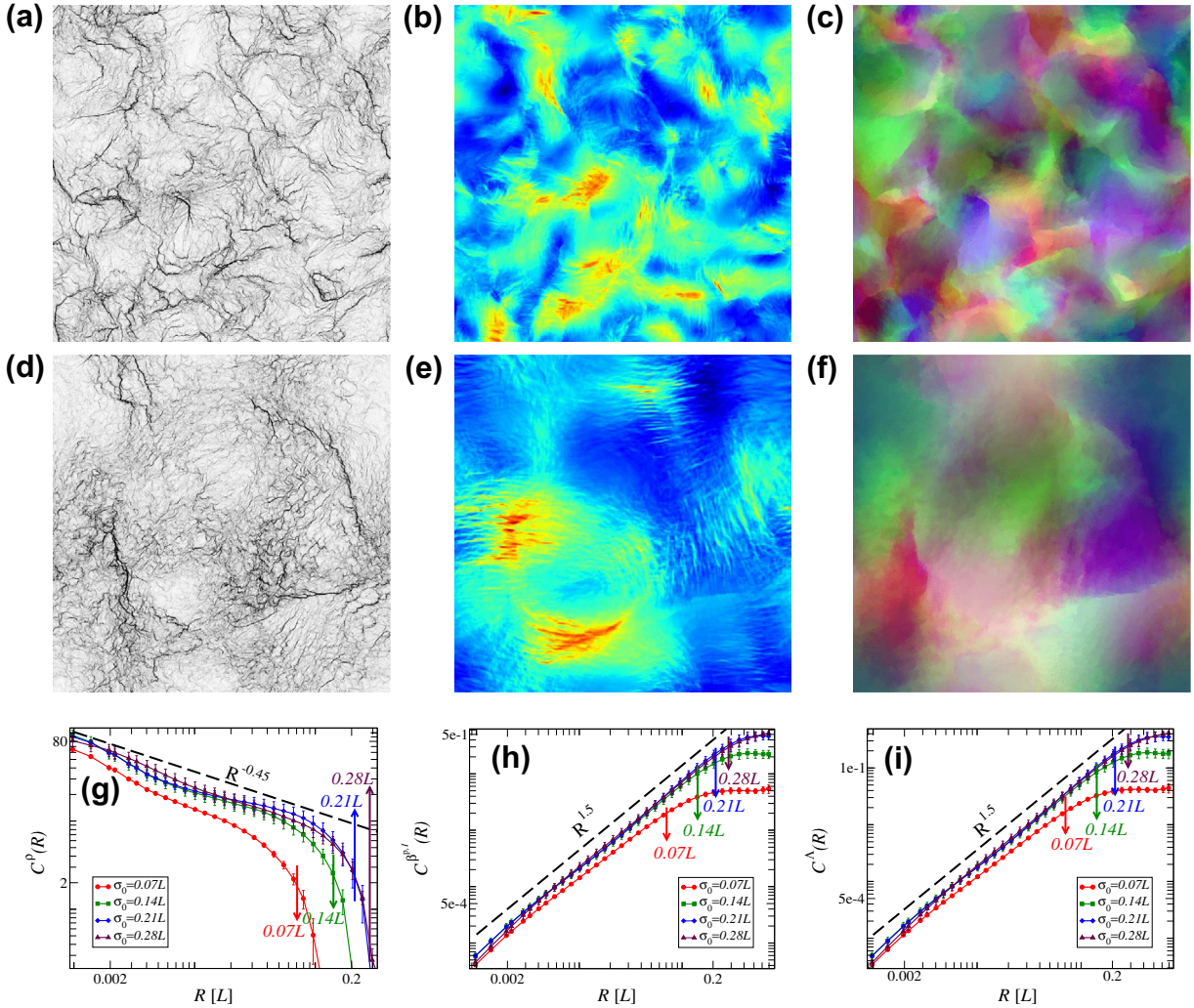
Fig. 7. Relaxation with various initial length scales in two dimensions. GNDs are not allowed to climb due to the constraint of a mobile dislocation population in these simulations. (a)–(c) are the net GND density map $|\varrho|$, the net plastic distortion $|\beta^p|$ (the warmer color indicating the larger distortion), and the crystalline orientation map in a fully-relaxed state evolved from an initial random plastic distortion with correlated length scale $0.07L$. They are compared to the same sequence of plots, (d)–(f), which are in the relaxed state with the initial length scale $0.21L$ three times as long. Notice the features with the longest wave length reflecting the initial distortion length scales. (g)–(i) are the scalar forms (discussed in Section 4.3) of correlation functions of the GND density ρ, the intrinsic plastic distortion $\beta^{p,l}$, and the crystalline orientation Λ for well-relaxed states with initial length scales varying from $0.07L$ to $0.28L$. They exhibit power laws independent of the initial length scales, with cutoffs set by the initial lengths. (The scaling relation among their critical exponents will be discussed in Section 5.)

4.3. Correlation functions

Hierarchical dislocation structures have been observed both experimentally (Kawasaki and Takeuchi, 1980; Mughrabi et al., 1986; Ungár et al., 1986; Schwink, 1992) and in our simulations (Chen et al., 2010). Early work analyzed experimental cellular structures using the fractal box counting method (Hähner et al., 1998) or by separating the systems into cells and analyzing their sizes and misorientations (Hughes et al., 1997; Hughes et al., 1998; Mika and Dawson, 1999; Hughes and Hansen, 2001). In our previous publication, we analyzed our simulated dislocation patterns using these two methods, and showed broad agreement with these experimental analyses (Chen et al., 2010). In fact, lack of the measurements of physical order parameters leads to incomplete characterization of the emergent self-similarity.[9] We will not pursue these methods here.

In our view, the emergent self-similarity should best be exhibited by the correlation functions of the order parameter fields, such as the GND density ρ, the plastic distortion β^p, and the crystalline orientation vector Λ. Here we focus on scalar invariants of the various tensor correlation functions.

---

[9] In these analyses of TEM micrographs, the authors must use an artificial cut-off to facilitate the analysis. This arbitrary scale obscures the scale-free nature behind the emergent dislocation patterns.

For the vector correlation function $\mathcal{C}_{ij}^\Lambda(\mathbf{x})$ (Eq. (52)), only the sum $\mathcal{C}_{ii}^\Lambda(\mathbf{x})$ is a scalar invariant under three dimensional rotations. For the tensor fields ρ and β^p, their two-point correlation functions are measured in terms of a complete set of three independent scalar invariants, which are indicated by 'tot' (total), 'per' (permutation), and 'tr' (trace). In searching for the explanation of the lack of scaling (Chen et al., 2010) for β^p (see Section 4.3.3 and E.1), we checked whether these independent invariants might scale independently. In fact, most of them share a single underlying critical exponent, except for the trace-type scalar invariant of the correlation function of $\beta^{p,I}$, which go to a constant in well-relaxed states, as discussed in Section 5.1.2.

4.3.1. Correlation function of crystalline orientation field

As dislocations self-organize themselves into complex structures, the relative differences of the crystalline orientations are correlated over a long length scale.

For a vector field, like the crystalline orientation Λ, the natural two-point correlation function is

$$\mathcal{C}_{ij}^\Lambda(\mathbf{x}) = \langle (\Lambda_i(\mathbf{x}) - \Lambda_i(0))(\Lambda_j(\mathbf{x}) - \Lambda_j(0)) \rangle = 2\langle \Lambda_i \Lambda_j \rangle - 2\langle \Lambda_i(\mathbf{x})\Lambda_j(0) \rangle. \tag{52}$$

Note that we correlate changes in Λ between two points. Just as for the height-height correlation function in surface growth (Chaikin and Lubensky, 1995), adding a constant to $\Lambda(\mathbf{x})$ (rotating the sample) leads to an equivalent configuration, so only differences in rotations can be meaningfully correlated.

It can be also described in Fourier space

$$\widetilde{\mathcal{C}}_{ij}^\Lambda(\mathbf{k}) = 2\langle \Lambda_i \Lambda_j \rangle (2\pi)^3 \delta(\mathbf{k}) - \frac{2}{V}\widetilde{\Lambda}_i(\mathbf{k})\widetilde{\Lambda}_j(-\mathbf{k}). \tag{53}$$

In an isotropic medium, we study the scalar invariant formed from $\mathcal{C}_{ij}^\Lambda$

$$\mathcal{C}^\Lambda(\mathbf{x}) = \mathcal{C}_{ii}^\Lambda(\mathbf{x}) = 2\langle \Lambda^2 \rangle - 2\langle \Lambda_i(\mathbf{x})\Lambda_i(0) \rangle. \tag{54}$$

Fig. 8 shows the correlation functions of crystalline orientations in both 1024^2 and 128^3 simulations. The large shift in critical exponents seen in 2D (Fig. 8(a)) for both CGD and GOD-LVP is not observed in the fully three dimensional simulations (Fig. 8(b)).

4.3.2. Correlation function of GND density field

As GNDs evolve into δ-shock singularities, the critical fluctuations of the GND density can be measured by the two-point correlation function $\mathcal{C}^\rho(\mathbf{x})$ of the GND density, which decays as the separating distance between two sites increases. The complete set of rotational invariants of the correlation function of ρ includes three scalar forms

$$\mathcal{C}_{tot}^\rho(\mathbf{x}) = \langle \rho_{ij}(\mathbf{x})\rho_{ij}(0) \rangle, \tag{55}$$

$$\mathcal{C}_{per}^\rho(\mathbf{x}) = \langle \rho_{ij}(\mathbf{x})\rho_{ji}(0) \rangle, \tag{56}$$

$$\mathcal{C}_{tr}^\rho(\mathbf{x}) = \langle \rho_{ii}(\mathbf{x})\rho_{jj}(0) \rangle. \tag{57}$$

Fig. 9 shows all the correlation functions of GND density in both 1024^2 and 128^3 simulations. These three scalar forms of the correlation functions of ρ exhibit the same critical exponent η, as listed in Table 1. Similar to the measurements of $\mathcal{C}^\Lambda$, the large shift in critical exponents seen in 2D (Fig. 9(a)) for both CGD and GOD-LVP is not observed in the fully three dimensional simulations (Fig. 9(b)).

4.3.3. Correlation function of plastic distortion field

The plastic distortion β^p is a mixture of both the divergence-free $\beta^{p,I}$ and the curl-free $\beta^{p,H}$. Fig. 10 shows that β^p does not appear to be scale invariant, as observed in our earlier work (Chen et al., 2010). It is crucial to study the correlations of the two physical fields, $\beta^{p,I}$ and $\beta^{p,H}$, separately.

Similarly to the crystalline orientation Λ, we correlate the differences between $\beta^{p,I}$ at neighboring points. The complete set of scalar invariants of correlation functions of $\beta^{p,I}$ thus includes the three scalar forms

$$\mathcal{C}_{tot}^{\beta^{p,I}}(\mathbf{x}) = \langle (\beta_{ij}^{p,I}(\mathbf{x}) - \beta_{ij}^{p,I}(0))(\beta_{ij}^{p,I}(\mathbf{x}) - \beta_{ij}^{p,I}(0)) \rangle = 2\langle \beta_{ij}^{p,I}\beta_{ij}^{p,I} \rangle - 2\langle \beta_{ij}^{p,I}(\mathbf{x})\beta_{ij}^{p,I}(0) \rangle; \tag{58}$$

$$\mathcal{C}_{per}^{\beta^{p,I}}(\mathbf{x}) = -\langle (\beta_{ij}^{p,I}(\mathbf{x}) - \beta_{ij}^{p,I}(0))(\beta_{ji}^{p,I}(\mathbf{x}) - \beta_{ji}^{p,I}(0)) \rangle = -2\langle \beta_{ij}^{p,I}\beta_{ji}^{p,I} \rangle + 2\langle \beta_{ij}^{p,I}(\mathbf{x})\beta_{ji}^{p,I}(0) \rangle; \tag{59}$$

$$\mathcal{C}_{tr}^{\beta^{p,I}}(\mathbf{x}) = \langle (\beta_{ii}^{p,I}(\mathbf{x}) - \beta_{ii}^{p,I}(0))(\beta_{jj}^{p,I}(\mathbf{x}) - \beta_{jj}^{p,I}(0)) \rangle = 2\langle \beta_{ii}^{p,I}\beta_{jj}^{p,I} \rangle - 2\langle \beta_{ii}^{p,I}(\mathbf{x})\beta_{jj}^{p,I}(0) \rangle; \tag{60}$$

where an overall minus sign is added to $\mathcal{C}_{per}^{\beta^{p,I}}$ so as to yield a positive measure.

In Fig. 11, the correlation functions of the intrinsic plastic distortion $\beta^{p,I}$ in both 1024^2 and 128^3 simulations exhibit a critical exponent σ'. These measured critical exponents are shown in Table 1. We discuss the less physically relevant case of $\beta^{p,H}$ in E.1, Fig. D.17.
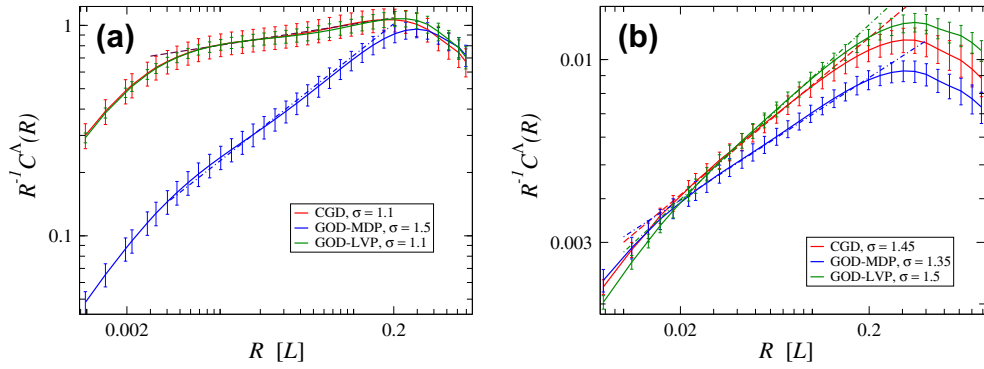
Fig. 8. Correlation functions of Λ in both two and three dimensions. In (a) and (b), red, blue, and green lines indicate CGD, GOD-MDP, and GOD-LVP simulations, respectively. *Left:* Correlation functions of Λ are measured in relaxed, unstrained 1024^2 systems; *Right:* These correlation functions are measured in relaxed, unstrained 128^3 systems. All dashed lines show estimated power laws quoted in Table 1. (For interpretation of the references to color in this figure legend, the reader is referred to the web version of this article.)
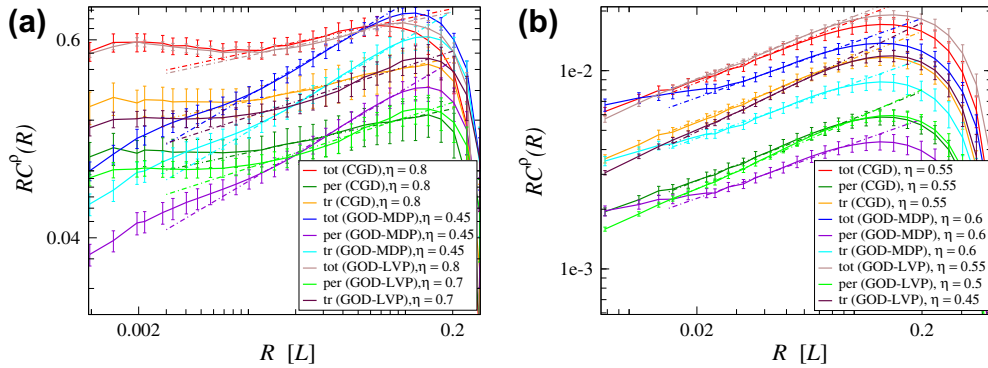
Fig. 9. Correlation functions of ϱ in both two and three dimensions. *Left:* (a) is measured in relaxed, unstrained 1024^2 systems; *Right:* (b) is measured in relaxed, unstrained 128^3 systems. All dashed lines show estimated power laws quoted in Table 1. Notice all three scalar forms of the correlation functions of GND density share the same power law.
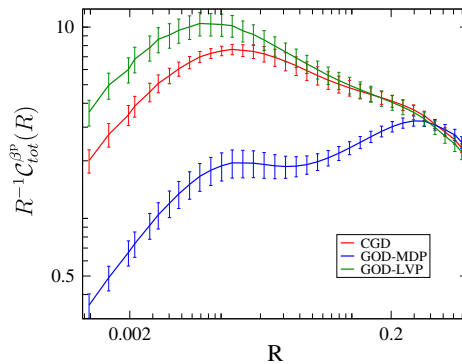
Fig. 10. Correlation functions of β^p in two dimensions. Red, blue, and green lines indicate CGD, GOD-MDP, and GOD-LVP simulations, respectively. None of these curves shows a convincing power law. (For interpretation of the references to color in this figure legend, the reader is referred to the web version of this article.)

5. Scaling theory

The emergent self-similar dislocation morphologies are characterized by the rotational invariants of correlation functions of physical observables, such as the GND density ρ, the crystalline orientation Λ, and the intrinsic plastic distortion $\beta^{p,l}$. Here we derive the relations expected between these correlation functions, and show that their critical exponents collapse into a single underlying one through a generic scaling theory.
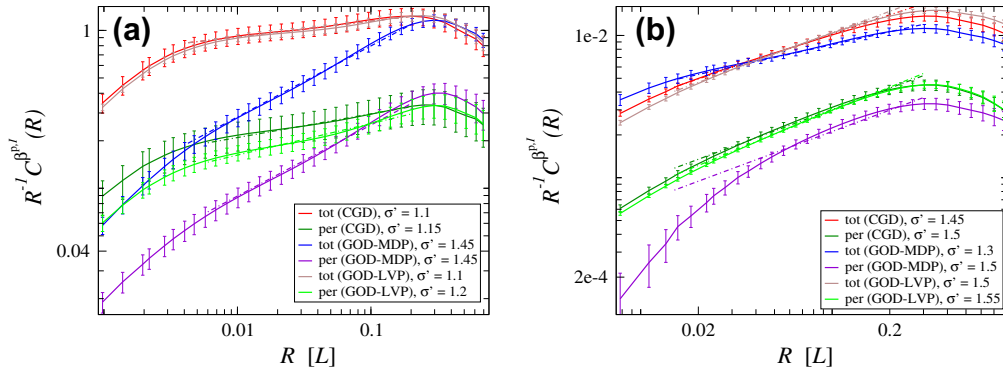
Fig. 11. Correlation functions of $\beta^{p,l}$ in both two and three dimensions. In (a) and (b), the correlation functions of the intrinsic part of plastic distortion field are shown. *Left:* (a) is measured in relaxed, unstrained 1024^2 systems; *Right:* (b) is measured in in relaxed, unstrained 128^3 systems. All dashed lines show estimated power laws quoted in Table 1. Notice that we omit the correlation functions of $\mathcal{C}_{tr}^{\beta^{p,l}}$, which are independent of distance, and unrelated to the emergent self-similarity, as shown in Section 5.1.2.

Table 1
Critical exponents for correlation functions at stress-free states. (C.F. and S.T. represent 'Correlation Functions' and 'Scaling Theory', respectively.)

C.F.	S.T.	Simulations					
		Climb and glide		Glide only (MDP)		LVP glide only (LVP)	
		2D (1024^2)	3D (128^3)	2D (1024^2)	3D (128^3)	2D (1024^2)	3D (128^3)
$\mathcal{C}_{tot}^{\rho}$	η	0.80 ± 0.30	0.55 ± 0.05	0.45 ± 0.25	0.60 ± 0.20	0.80 ± 0.30	0.55 ± 0.05
$\mathcal{C}_{per}^{\rho}$	η	0.80 ± 0.20	0.55 ± 0.05	0.45 ± 0.20	0.60 ± 0.20	0.70 ± 0.30	0.50 ± 0.05
$\mathcal{C}_{tr}^{\rho}$	η	0.80 ± 0.20	0.55 ± 0.05	0.45 ± 0.20	0.60 ± 0.10	0.70 ± 0.30	0.45 ± 0.05
$\mathcal{C}^{\Lambda}$	$2-\eta$	1.10 ± 0.65	1.45 ± 0.25	1.50 ± 0.30	1.35 ± 0.25	1.10 ± 0.65	1.50 ± 0.25
$\mathcal{C}_{tot}^{\beta^{p,l}}$	$2-\eta$	1.10 ± 0.60	1.45 ± 0.15	1.45 ± 0.25	1.30 ± 0.20	1.10 ± 0.60	1.50 ± 0.20
$\mathcal{C}_{per}^{\beta^{p,l}}$	$2-\eta$	1.15 ± 0.45	1.50 ± 0.25	1.45 ± 0.25	1.50 ± 0.50	1.20 ± 0.45	1.55 ± 0.25

In our model, the initial elastic stresses are relaxed via dislocation motion, leading to the formation of cellular structures. In the limit of slow imposed deformations, the elastic stress goes to zero in our model. We will use the absence of external stress to simplify our correlation function relations. (Some relations can be valid regardless of the existence of residual stress.) Those relations that hold only in stress-free states will be labeled 'sf'; they will be applicable in analyzing experiments only insofar as residual stresses are small.

5.1. Relations between correlation functions

5.1.1. $\mathcal{C}^{\rho}$ and $\mathcal{C}^{\Lambda}$

For a stress-free state, we thus ignore the elastic strain term in Eq. (14) and write in Fourier space

$$\widetilde{\rho}_{ij}(\mathbf{k}) \overset{sf}{=} -ik_j \widetilde{\Lambda}_i(\mathbf{k}) + i\delta_{ij} k_k \widetilde{\Lambda}_k(\mathbf{k}). \tag{61}$$

First, we can substitute Eq. (61) into the Fourier-transformed form of the correlation function Eq. (55)

$$\widetilde{\mathcal{C}}_{tot}^{\rho}(\mathbf{k}) \overset{sf}{=} \frac{1}{V}\left(-ik_j \widetilde{\Lambda}_i(\mathbf{k}) + i\delta_{ij} k_k \widetilde{\Lambda}_k(\mathbf{k})\right)\left(ik_j \widetilde{\Lambda}_i(-\mathbf{k}) - i\delta_{ij} k_m \widetilde{\Lambda}_m(-\mathbf{k})\right) \overset{sf}{=} \frac{1}{V}(\delta_{ij} k^2 + k_i k_j)\widetilde{\Lambda}_i(\mathbf{k})\widetilde{\Lambda}_j(-\mathbf{k}). \tag{62}$$

Multiplying both sides of Eq. (53) by $(\delta_{ij}k^2 + k_i k_j)$ gives

$$(\delta_{ij}k^2 + k_i k_j)\widetilde{\mathcal{C}}_{ij}^{\Lambda}(\mathbf{k}) \overset{sf}{=} -\frac{2}{V}(\delta_{ij}k^2 + k_i k_j)\widetilde{\Lambda}_i(\mathbf{k})\widetilde{\Lambda}_j(-\mathbf{k}). \tag{63}$$

Comparing Eq. (63) and Eq. (62), we may write $\widetilde{\mathcal{C}}_{tot}^{\rho}$ in terms of $\widetilde{\mathcal{C}}_{ij}^{\Lambda}$ as

$$\widetilde{\mathcal{C}}_{tot}^{\rho}(\mathbf{k}) \overset{sf}{=} -\frac{1}{2}(\delta_{ij}k^2 + k_i k_j)\widetilde{\mathcal{C}}_{ij}^{\Lambda}(\mathbf{k}). \tag{64}$$

Second, we can substitute Eq. (61) into the Fourier-transformed form of the correlation function Eq. (56)

$$\widetilde{\mathcal{C}}_{per}^{\rho}(\mathbf{k}) \overset{sf}{=} \frac{2}{V} k_i k_j \widetilde{\Lambda}_i(\mathbf{k}) \widetilde{\Lambda}_j(-\mathbf{k}). \tag{65}$$

Multiplying both sides of Eq. (53) by $k_i k_j$ and comparing with Eq. (65) gives

$$\widetilde{\mathcal{C}}_{per}^{\rho}(\mathbf{k}) \overset{sf}{=} -k_i k_j \widetilde{\mathcal{C}}_{ij}^{\Lambda}(\mathbf{k}). \tag{66}$$

Finally, we substitute Eq. (61) into the Fourier-transformed form of the correlation function Eq. (57)

$$\widetilde{\mathcal{C}}_{tr}^{\rho}(\mathbf{k}) \overset{sf}{=} \frac{4}{V} k_i k_j \widetilde{\Lambda}_i(\mathbf{k}) \widetilde{\Lambda}_j(-\mathbf{k}). \tag{67}$$

Repeating the same procedure of deriving $\widetilde{\mathcal{C}}_{per}^{\rho}$, we write $\widetilde{\mathcal{C}}_{tr}^{\rho}$ in terms of $\widetilde{\mathcal{C}}_{ij}^{\Lambda}$ as

$$\widetilde{\mathcal{C}}_{tr}^{\rho}(\mathbf{k}) \overset{sf}{=} -2k_i k_j \widetilde{\mathcal{C}}_{ij}^{\Lambda}(\mathbf{k}). \tag{68}$$

Through an inverse Fourier transform, we convert Eqs. (64), (66), and (68) back to real space to find

$$\mathcal{C}_{tot}^{\rho}(\mathbf{x}) \overset{sf}{=} \frac{1}{2}\partial^2 \mathcal{C}^{\Lambda}(\mathbf{x}) + \frac{1}{2}\partial_i \partial_j \mathcal{C}_{ij}^{\Lambda}(\mathbf{x}), \tag{69}$$

$$\mathcal{C}_{per}^{\rho}(\mathbf{x}) \overset{sf}{=} \partial_i \partial_j \mathcal{C}_{ij}^{\Lambda}(\mathbf{x}), \tag{70}$$

$$\mathcal{C}_{tr}^{\rho}(\mathbf{x}) \overset{sf}{=} 2\partial_i \partial_j \mathcal{C}_{ij}^{\Lambda}(\mathbf{x}). \tag{71}$$

5.1.2. $\mathcal{C}^{\beta^{p,I}}$ and $\mathcal{C}^{\Lambda}$

The intrinsic part of the plastic distortion field is directly related to the GND density field. In stress-free states, the crystalline orientation vector can fully describe the GND density. We thus can connect $\mathcal{C}^{\beta^{p,I}}$ to $\mathcal{C}^{\Lambda}$.

First, substituting $\widetilde{\beta}_{ij}^{p,I} = -i\varepsilon_{ilm} k_l \widetilde{\rho}_{mj}/k^2$ into the Fourier-transformed form of Eq. (58) gives

$$\begin{aligned}\widetilde{\mathcal{C}}_{tot}^{\beta^{p,I}}(\mathbf{k}) &= 2\left\langle \beta_{ij}^{p,I} \beta_{ij}^{p,I} \right\rangle (2\pi)^3 \delta(\mathbf{k}) - \frac{2}{V}\left(-i\epsilon_{ilm}\frac{k_l}{k^2}\widetilde{\rho}_{mj}(\mathbf{k}) \right)\left(i\epsilon_{ist}\frac{k_s}{k^2}\widetilde{\rho}_{tj}(-\mathbf{k}) \right) \\ &= 2\left\langle \beta_{ij}^{p,I} \beta_{ij}^{p,I} \right\rangle (2\pi)^3 \delta(\mathbf{k}) - \frac{2}{k^2}\left(\frac{1}{V}\widetilde{\rho}_{mj}(\mathbf{k})\widetilde{\rho}_{mj}(-\mathbf{k}) \right). \end{aligned} \tag{72}$$

During this derivation, some terms vanish due to the geometrical constraint on ρ, Eq. (6). Multiplying $-k^2/2$ on both sides of Eq. (72) and applying the Fourier-transformed form of Eq. (55) gives

$$-\frac{k^2}{2}\widetilde{\mathcal{C}}_{tot}^{\beta^{p,I}}(\mathbf{k}) = \widetilde{\mathcal{C}}_{tot}^{\rho}(\mathbf{k}). \tag{73}$$

In stress-free states, we can substitute Eq. (64) into Eq. (73)

$$-\frac{k^2}{2}\widetilde{\mathcal{C}}_{tot}^{\beta^{p,I}}(\mathbf{k}) \overset{sf}{=} \widetilde{\mathcal{C}}_{tot}^{\rho,sf}(\mathbf{k}) = -\frac{1}{2}\left(\delta_{ij}k^2 + k_i k_j \right)\widetilde{\mathcal{C}}_{ij}^{\Lambda}(\mathbf{k}), \tag{74}$$

which is rewritten after multiplying $-2/k^2$ on both sides

$$\widetilde{\mathcal{C}}_{tot}^{\beta^{p,I}}(\mathbf{k}) \overset{sf}{=} \widetilde{\mathcal{C}}^{\Lambda}(\mathbf{k}) + \frac{k_i k_j}{k^2}\widetilde{\mathcal{C}}_{ij}^{\Lambda}(\mathbf{k}). \tag{75}$$

Second, substituting $\widetilde{\beta}_{ij}^{p,I} = -i\varepsilon_{ilm} k_l \widetilde{\rho}_{mj}/k^2$ into the Fourier-transformed form of Eq. (59) gives

$$\begin{aligned}\widetilde{\mathcal{C}}_{per}^{\beta^{p,I}}(\mathbf{k}) &= -2\left\langle \beta_{ij}^{p,I} \beta_{ji}^{p,I} \right\rangle (2\pi)^3 \delta(\mathbf{k}) + \frac{2}{V}\left(-i\epsilon_{ilm}\frac{k_l}{k^2}\widetilde{\rho}_{mj}(\mathbf{k}) \right)\left(i\epsilon_{jst}\frac{k_s}{k^2}\widetilde{\rho}_{ti}(-\mathbf{k}) \right) \\ &= -2\left\langle \beta_{ij}^{p,I} \beta_{ji}^{p,I} \right\rangle (2\pi)^3 \delta(\mathbf{k}) - \frac{2}{Vk^4}k_i k_j \widetilde{\rho}_{mj}(\mathbf{k})\widetilde{\rho}_{mi}(-\mathbf{k}) + \frac{2}{k^2}\widetilde{\mathcal{C}}_{tot}^{\rho}(\mathbf{k}) - \frac{2}{k^2}\widetilde{\mathcal{C}}_{tr}^{\rho}(\mathbf{k}), \end{aligned} \tag{76}$$

where we skip straightforward but tedious expansions and the geometrical constraint on ρ, Eq. (6). Notice that this relation is correct even in the presence of stress.

In stress-free states, we substitute Eqs. (61), (64), (68) into Eq. (76), and ignore the constant zero wavelength term

$$\begin{aligned}\widetilde{\mathcal{C}}_{per}^{\beta^{p,I}}(\mathbf{k}) &\overset{sf}{=} -\frac{2k_i k_j}{Vk^4}\left(-ik_j\widetilde{\Lambda}_m(\mathbf{k}) + i\delta_{mj}k_k\widetilde{\Lambda}_k(\mathbf{k}) \right)\left(ik_i\widetilde{\Lambda}_m(-\mathbf{k}) - i\delta_{mi}k_n\widetilde{\Lambda}_n(-\mathbf{k}) \right) - \frac{1}{k^2}(k^2\delta_{ij} + k_i k_j)\widetilde{\mathcal{C}}_{ij}^{\Lambda}(\mathbf{k}) + \frac{4}{k^2}k_i k_j \widetilde{\mathcal{C}}_{ij}^{\Lambda}(\mathbf{k}) \\ &\times \overset{sf}{=} 2\frac{k_i k_j}{k^2}\widetilde{\mathcal{C}}_{ij}^{\Lambda}(\mathbf{k}). \end{aligned} \tag{77}$$

Finally, substituting $\widetilde{\beta}_{ij}^{p,I} = -i\varepsilon_{ilm} k_l \widetilde{\rho}_{mj}/k^2$ into the Fourier-transformed form of Eq. (60) gives

$$\widetilde{\mathcal{C}}_{tr}^{\beta^{\mathrm{p,I}}}(\mathbf{k}) = 2\langle\beta_{ii}^{\mathrm{p,I}}\beta_{jj}^{\mathrm{p,I}}\rangle(2\pi)^3\delta(\mathbf{k}) - \frac{2}{V}\left(-i\epsilon_{ilm}\frac{k_l}{k^2}\widetilde{\rho}_{mi}(\mathbf{k})\right)\left(i\epsilon_{jst}\frac{k_s}{k^2}\widetilde{\rho}_{tj}(-\mathbf{k})\right)$$

$$= 2\left\langle\beta_{ii}^{\mathrm{p,I}}\beta_{jj}^{\mathrm{p,I}}\right\rangle(2\pi)^3\delta(\mathbf{k}) + \frac{2}{Vk^4}k_ik_j\widetilde{\rho}_{mi}(\mathbf{k})\widetilde{\rho}_{mj}(-\mathbf{k}) - \frac{2}{k^2}\widetilde{\mathcal{C}}_{tot}^{\rho}(\mathbf{k}) + \frac{2}{k^2}\widetilde{\mathcal{C}}_{per}^{\rho}(\mathbf{k}), \tag{78}$$

valid in the presence of stress. Here we repeat a similar procedure as was used to derive in Eq. (76).

In stress-free states, we substitute Eqs. (61), (64), (66) into Eq. (78)

$$\widetilde{\mathcal{C}}_{tr}^{\beta^{\mathrm{p,I}}}(\mathbf{k}) \overset{sf}{=} 2\langle\beta_{ii}^{\mathrm{p,I}}\beta_{jj}^{\mathrm{p,I}}\rangle(2\pi)^3\delta(\mathbf{k}) + \frac{1}{k^2}(k^2\delta_{ij} + k_ik_j)\widetilde{\mathcal{C}}_{ij}^{\Lambda}(\mathbf{k}) - \frac{2}{k^2}k_ik_j\widetilde{\mathcal{C}}_{ij}^{\Lambda}(\mathbf{k})$$

$$+ \frac{2k_ik_j}{Vk^4}\left(-ik_i\widetilde{\Lambda}_m(\mathbf{k}) + i\delta_{mi}k_k\widetilde{\Lambda}_k(\mathbf{k})\right)\left(ik_j\widetilde{\Lambda}_m(-\mathbf{k}) - i\delta_{mj}k_n\widetilde{\Lambda}_n(-\mathbf{k})\right) \overset{sf}{=} 2\langle\beta_{ii}^{\mathrm{p,I}}\beta_{jj}^{\mathrm{p,I}}\rangle(2\pi)^3\delta(\mathbf{k}), \tag{79}$$

which is a trivial constant in space.

Through an inverse Fourier transform, Eqs. (75), (77), and (79) can be converted back to real space, giving

$$\mathcal{C}_{tot}^{\beta^{\mathrm{p,I}}}(\mathbf{x}) \overset{sf}{=} \mathcal{C}^{\Lambda}(\mathbf{x}) + \frac{1}{4\pi}\int d^3\mathbf{x}'\left(\frac{\delta_{ij}}{R^3} - 3\frac{R_iR_j}{R^5}\right)\mathcal{C}_{ij}^{\Lambda}(\mathbf{x}'), \tag{80}$$

$$\mathcal{C}_{per}^{\beta^{\mathrm{p,I}}}(\mathbf{x}) \overset{sf}{=} \frac{1}{2\pi}\int d^3\mathbf{x}'\left(\frac{\delta_{ij}}{R^3} - 3\frac{R_iR_j}{R^5}\right)\mathcal{C}_{ij}^{\Lambda}(\mathbf{x}'), \tag{81}$$

$$\mathcal{C}_{tr}^{\beta^{\mathrm{p,I}}}(\mathbf{x}) \overset{sf}{=} 2\int d^3\mathbf{x}'\beta_{ii}^{\mathrm{p,I}}(\mathbf{x}')\beta_{jj}^{\mathrm{p,I}}(\mathbf{x}') = 2\left\langle\beta_{ii}^{\mathrm{p,I}}\beta_{jj}^{\mathrm{p,I}}\right\rangle, \tag{82}$$

where $\mathbf{R} = \mathbf{x}' - \mathbf{x}$. According to Eqs. (75) and (77), we can extract a relation

$$\mathcal{C}_{per}^{\beta^{\mathrm{p,I}}}(\mathbf{x}) - 2\mathcal{C}_{tot}^{\beta^{\mathrm{p,I}}}(\mathbf{x}) + 2\mathcal{C}^{\Lambda}(\mathbf{x}) \overset{sf}{=} const. \tag{83}$$

We can convert Eq. (73) through an inverse Fourier transform

$$\mathcal{C}_{tot}^{\rho}(\mathbf{x}) = \frac{1}{2}\partial^2\mathcal{C}_{tot}^{\beta^{\mathrm{p,I}}}(\mathbf{x}), \tag{84}$$

or

$$\mathcal{C}_{tot}^{\beta^{\mathrm{p,I}}}(\mathbf{x}) = -\frac{1}{2\pi}\int d^3\mathbf{x}'\frac{\mathcal{C}_{tot}^{\rho}(\mathbf{x}')}{R}, \tag{85}$$

valid in the presence of residual stress.

5.2. Critical exponent relations

When the self-similar dislocation structures emerge, the correlation functions of all physical quantities are expected to exhibit scale-free power laws. We consider the simplest possible scenario, where single variable scaling is present to reveal the minimal number of underlying critical exponents.

First, we define the critical exponent η as the power law describing the asymptotic decay of $\mathcal{C}_{tot}^{\rho}(\mathbf{x}) \sim |\mathbf{x}|^{-\eta}$, one of the correlation functions for the GND density tensor (summed over components). If we rescale the spatial variable $\mathbf{x}$ by a factor b, the correlation function $\mathcal{C}^{\rho}$ is rescaled by the power law as

$$\mathcal{C}_{tot}^{\rho}(b\mathbf{x}) = b^{-\eta}\mathcal{C}_{tot}^{\rho}(\mathbf{x}). \tag{86}$$

Similarly, the correlation function of the crystalline orientation field Λ is described by a power law, $\mathcal{C}^{\Lambda}(\mathbf{x}) \sim |\mathbf{x}|^{\sigma}$, where σ is its critical exponent. We repeat the rescaling by the same factor b

$$\mathcal{C}^{\Lambda}(b\mathbf{x}) = b^{\sigma}\mathcal{C}^{\Lambda}(\mathbf{x}). \tag{87}$$

Since $\mathcal{C}_{tot}^{\rho}$ can be written in terms of $\mathcal{C}^{\Lambda}$, Eq. (69), we rescale this relation by the same factor b

$$\mathcal{C}_{tot}^{\rho}(b\mathbf{x}) \overset{sf}{=} \frac{1}{2}\left[\frac{\partial}{b}\right]^2\mathcal{C}^{\Lambda}(b\mathbf{x}) + \frac{1}{2}\left[\frac{\partial_i}{b}\right]\left[\frac{\partial_j}{b}\right]\mathcal{C}_{ij}^{\Lambda}(b\mathbf{x}). \tag{88}$$

Substituting Eq. (87) into Eq. (88) gives

$$\mathcal{C}_{tot}^{\rho}(b\mathbf{x}) \overset{sf}{=} b^{\sigma-2}\left[\frac{1}{2}\partial^2\mathcal{C}^{\Lambda}(\mathbf{x}) + \frac{1}{2}\partial_i\partial_j\mathcal{C}_{ij}^{\Lambda}(\mathbf{x})\right] \overset{sf}{=} b^{\sigma-2}\mathcal{C}_{tot}^{\rho}(\mathbf{x}). \tag{89}$$

Comparing with Eq. (86) gives a relation between σ and η

$$\sigma = 2 - \eta. \tag{90}$$

We can repeat the same renormalization group procedure to analyze the critical exponents of the other two scalar forms of the correlation functions of the GND density field. Clearly, $\mathcal{C}_{per}^{\rho}$ and $\mathcal{C}_{tr}^{\rho}$ share the same critical exponent η with $\mathcal{C}_{tot}^{\rho}$.

Also, we can define the critical exponent σ' as the power law describing the asymptotic growth of $\mathcal{C}_{tot}^{\beta^{p,I}}(\mathbf{x}) \sim |\mathbf{x}|^{\sigma'}$, one of the correlation functions for the intrinsic part of the plastic distortion field. We can rescale the correlation function $\mathcal{C}^{\beta^{p,I}}$

$$\mathcal{C}_{tot}^{\beta^{p,I}}(b\mathbf{x}) = b^{\sigma'}\mathcal{C}_{tot}^{\beta^{p,I}}(\mathbf{x}). \tag{91}$$

We rescale the relation Eq. (84) by the same factor b, and substitute Eq. (91) into it

$$\mathcal{C}_{tot}^{\rho}(b\mathbf{x}) = \frac{1}{2}\left[\frac{\partial}{b}\right]^2 \mathcal{C}_{tot}^{\beta^{p,I}}(b\mathbf{x}) = b^{\sigma'-2}\left[\frac{1}{2}\partial^2 \mathcal{C}_{tot}^{\beta^{p,I}}(\mathbf{x})\right] = b^{\sigma'-2}\mathcal{C}_{tot}^{\rho}(\mathbf{x}). \tag{92}$$

Comparing with Eq. (86) also gives a relation between σ' and η

$$\sigma' = 2 - \eta. \tag{93}$$

Since both $\mathcal{C}_{tot}^{\beta^{p,I}}$ and $\mathcal{C}^{\Lambda}$ share the same critical exponent $2 - \eta$, it is clear that $\mathcal{C}_{per}^{\beta^{p,I}}$, the other scalar form of the correlation functions of the intrinsic plastic distortion field, also shares this critical exponent, according to Eq. (83).

Thus the correlation functions of three physical quantities (the GND density ρ, the crystalline orientation Λ, and the intrinsic plastic distortion $\beta^{p,I}$) all share the same underlying universal critical exponent η for self-similar morphologies, in the case of zero residual stress, and still hold in the limit of slow imposed deformation. Table 1 verifies the existence of single underlying critical exponent in both two and three dimensional simulations for each type of dynamics. Imposed strain, studied in Chen et al., 2010, could in principle change η, but the scaling relations derived here should still apply. The strain, of course, breaks the isotropic symmetry, allowing even more allowed correlation functions to be measured.

5.3. Coarse graining, correlation functions, and cutoffs

Our dislocation density ρ, as discussed in Section 3, is a coarse-grained average over some distance Σ – taking the discrete microscopic dislocations and yielding a continuum field expressing their flux in different directions. Our power laws and scaling will be cut off in some way at this coarse-graining scale. For our simulations, the correlation functions extend down to a few times the numerical grid spacing (depending on the numerical diffusion in the algorithm we use). For experiments, the correlation functions will be cut off in ways that are determined by the instrumental resolution. Since the process of coarse-graining is at the heart of the renormalization-group methods we rely upon to explain the emergent scale invariance in our model, we make an initial exploration here of how coarse-graining by the Gaussian blur of Eq. (47) and Eq. (48) affects the $\rho^{\Sigma} - \rho^{\Sigma}$ correlation function.

Following Eq. (47),

$$\mathcal{C}_{tot}^{\rho^{\Sigma}}(\mathbf{x}) = \left\langle \rho_{ij}^{\Sigma}(\mathbf{x})\rho_{ij}^{\Sigma}(0) \right\rangle = \frac{1}{V}\frac{1}{(2\pi\Sigma^2)^3}\int d^3\mathbf{y}\int d^3\mathbf{z}\rho_{ij}^0(\mathbf{y}+\mathbf{z})e^{-z^2/(2\Sigma^2)}\int d^3\mathbf{z}'\rho_{ij}^0(\mathbf{y}+\mathbf{x}+\mathbf{z}')e^{-z'^2/(2\Sigma^2)}. \tag{94}$$

By changing variables $\mathbf{s} = \mathbf{y} + \mathbf{z}$ and $\boldsymbol{\Delta} = \mathbf{z}' - \mathbf{z}$, we integrate out the variable $\mathbf{z}$ of Eq. (94),

$$\mathcal{C}_{tot}^{\rho^{\Sigma}}(\mathbf{x}) = \frac{1}{8\pi^{3/2}\Sigma^3}\frac{1}{V}\int d^3\boldsymbol{\Delta}\int d^3\mathbf{s}\rho_{ij}^0(\mathbf{s})\rho_{ij}^0(\mathbf{s}+\boldsymbol{\Delta}+\mathbf{x})e^{-\Delta^2/(4\Sigma^2)} = \frac{1}{8\pi^{3/2}\Sigma^3}\int d^3\boldsymbol{\Delta}\mathcal{C}_{tot}^0(\mathbf{x}+\boldsymbol{\Delta})e^{-\Delta^2/(4\Sigma^2)}. \tag{95}$$

In our simulating system, the correlation functions of GND density can be described by a power-law Eq. (86), $\mathcal{C}_{tot}^{\rho}(\mathbf{x}) = g|\mathbf{x}|^{-\eta}$, where g is a constant. Thus, Eq. (95) is

$$\mathcal{C}_{tot}^{\rho^{\Sigma}}(\mathbf{x}) = \frac{g}{8\pi^{3/2}\Sigma^3}\int d^3\boldsymbol{\Delta}|\mathbf{x}+\boldsymbol{\Delta}|^{-\eta}e^{-\Delta^2/(4\Sigma^2)}. \tag{96}$$
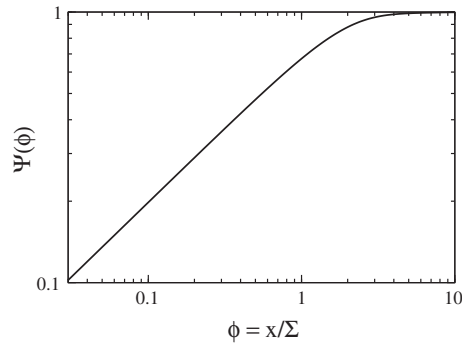
This correlation function of the coarse-grained GND density at the given scale Σ is a power-law smeared by a Gaussian distribution.

Since the scalar field of the coarse-grained correlation function is rotational invariant, we assume that $\mathbf{x}$ is aligned along the x axis, $\mathbf{x} = (x, 0, 0)$. Then we could evaluate the integral of Eq. (96) in cylindrical coordinates $\boldsymbol{\Delta} = (X, r, \theta)$

$$\begin{aligned}\mathcal{C}_{tot}^{\rho^{\Sigma}}(x, \Sigma) &= \frac{g}{8\pi^{3/2}\Sigma^3}\int_0^{\infty}2\pi r dr\int_{-\infty}^{\infty}dX|(x+X)^2+r^2|^{-\eta/2}e^{-(X^2+r^2)/(4\Sigma^2)}\\ &= \frac{g}{2^{1+\eta}\pi^{1/2}}\Sigma^{-\eta-1}\int_{-\infty}^{\infty}dXe^{(X^2+2xX)/(4\Sigma^2)}\Gamma\left(1-\eta/2, (x+X)^2/(4\Sigma^2)\right).\end{aligned} \tag{97}$$

We can rewrite this coarse-grained correlation functions Eq. (97) as a power-law multiplied by a scaling function

$$\mathcal{C}_{tot}^{\rho^{\Sigma}}(x, \Sigma) = g|x|^{-\eta}\Psi(x/\Sigma), \tag{98}$$

Fig. 12. Scaling function of the correlation function of coarse-grained GND density ρ^Σ. We calculate the correlation function of the coarse-grained GND density at the given scale Σ. Theoretically, its scaling function remains a power-law at the small coarse-graining length scale, and flattens out to be 1 as the correlation length of the system is far larger than the coarse-graining scale.

where the scaling function $\Psi(\cdot)$ (Fig. 12) equals

$$\Psi(\phi) = \frac{1}{2^{1+\eta}\pi^{1/2}}|\phi|^\eta \int_{-\infty}^{\infty} ds\, e^{s(s+2\phi)/4}\Gamma\left(1 - \eta/2, (s+\phi)^2/4\right). \tag{99}$$

6. Conclusion

In our earlier works (Limkumnerd and Sethna, 2006; Chen et al., 2010; Choi et al., 2012b), we have proposed a flexible framework of CDD to study complex mesoscale phenomena of collective dislocation motion. Traditionally, deterministic CDDs have missed the experimentally ubiquitous feature of cellular pattern formation. Our CDD models have made progress in that respect. In the beginning, we focused our efforts on describing coarse-grained dislocations that naturally develop dislocation cellular structures in ways that are consistent with experimental observations of scale invariance and fractality, a target achieved in Chen et al. (2010). However, that paper studied only 2D, instead of the more realistic 3D.

In this manuscript, we go further in many aspects of the theory extending the results of our previous work:

We provide a derivation of our theory that explains the differences with traditional theories of plasticity. In addition to our previously studied climb-glide (CGD) and glide-only (GOD-MDP) models, we extend our construction in order to incorporate vacancies, and re-derive (Acharya and Roy, 2006) a different glide-only dynamics (GOD-LVP) which we show exhibits very similar behavior in 2D to our CGD model. It is worth mentioning that in this way, the GOD-LVP and the CGD dynamics become statistically similar in 2D, while the previously studied, less physical, GOD-MDP model provides rather different behavior in 2D (Chen et al., 2010).

We present 3D simulation results here for the first time, showing qualitatively different behavior from that of 2D. In 3D, all three types of dynamics – CGD, GOD-MDP and GOD-LVP – show similar non-trivial fractal patterns and scaling dimensions. Thus our 3D analysis shows that the flatter 'grain boundaries' we observe in the 2D simulations are not intrinsic to our dynamics, but are an artifact of the artificial z-independent initial conditions. Experimentally, grain boundaries are indeed flatter and cleaner than cell walls, and our theory no longer provides a new explanation for this distinction. We expect that the dislocation core energies left out of our model would flatten the walls, and that adding disorder or entanglement would prevent the low-temperature glide-only dynamics from flattening as much.

We also fully describe, in a statistical sense, multiple correlation functions – the local orientation, the plastic distortion, the GND density – their symmetries and their mutual scaling relations. Correlation functions of important physical quantities are categorized and analytically shown to share one stress-free exponent. The anomaly in the correlation functions of β^p, which was left as a question in our previous publication (Chen et al., 2010), has been discussed and explained. All of these correlation functions and properties are verified with the numerical results of the dynamics that we extensively discussed.

As discussed in Section 1, our model is an immensely simplified caricature of the deformation of real materials. How does it connect to reality?

First, we show that a model for which the dynamics is driven only by elastic strain produces realistic cell wall structures even while ignoring slip systems, crystalline anisotropy (Hughes et al., 1998), pinning, junction formation, and SSDs. The fact that low-energy dislocation structures (LEDS) provides natural explanations for many properties of these structures has long been emphasized by Kuhlmann-Wilsdorf (1987). Intermittent flow, forest interactions, and pinning will in general impede access to low energy states. These real-world features, our model suggests, can be important for the morphology of the cell wall structures but are not the root cause of their formation nor of their evolution under stress (discussed in previous work (Chen et al., 2010)).

One must note, however, that strain energy minimization does not provide the explanation for wall structures in our model material. Indeed, there is an immense space of dislocation densities which make the strain energy zero (Limkumnerd

and Sethna, 2007), including many continuous densities. Our dynamics relaxes into a small subset of these allowed structures – it is the dynamics that leads to cell structure formation here, not purely the energy. In discrete dislocation simulations and real materials, the quantization of the Burgers vector leads to a weak logarithmic energetic preference for sharp walls. This $-\mu\mathbf{b}/(4\pi(1-v))\theta\log\theta$ energy of low-angle grain boundaries yields a $\log 2$ preference for one wall of angle θ rather than two walls of angle $\theta/2$. This leads to a 'zipping' together of low angle grain boundaries. Since $\mathbf{b} \rightarrow 0$ in a continuum theory, this preference is missing from our model. Yet, we still find cell wall formation suggesting that such mechanisms are not central to cell wall formation.

Second, how should we connect our fractal cell wall structures with those (fractal or non-fractal) seen in experiments? Many qualitatively different kinds of cellular structures are seen in experiments – variously termed cell block structures, mosaic structures, ordinary cellular structures,... Hansen et al. (2011) recently categorized these structures into three types, and argue that the orientation of the stress with respect to the crystalline axes largely determines which morphology is exhibited. The cellular structures in our model, which ignores crystalline anisotropy, likely are the theoretical progenitors of all of these morphologies. In particular, Hansen's type 1 and type 3 structures incorporate both 'geometrically necessary' and 'incidental dislocation' boundaries (GNBs and IDBs), while type 2 structures incorporate only the latter. Our simulations cannot distinguish between these two types, and indeed qualitatively look similar to Hansen's type 2 structures. One should note that the names of these boundaries are misleading – the 'incidental' boundaries do mediate geometrical rotations, with the type 2 boundaries at a given strain having similar average misorientations to the geometrically necessary boundaries of type 1 structures (Hansen et al., 2011, Fig. 8). It is commonly asserted that the IDBs are formed by statistical trapping of stored dislocations; our model suggests that stochasticity is not necessary for their formation.

Third, how is our model compatible with traditional plasticity, which focuses on the total density of dislocation lines? Our model evolves the net dislocation density, ignoring the *geometrically unnecessary* or *statistically stored* dislocations with canceling Burgers vectors. These latter dislocations are important for yield stress and work hardening on macroscales, but are invisible to our theory (since they do not generate stress). Insofar as the cancelation of Burgers vectors on the macroscale is due to cell walls of opposing misorientations on the mesoscale, there needs to be no conflict here. Also our model remains agnostic about whether cell boundaries include significant components of geometrically unnecessary dislocations. However, our model does assume that the driving force for cell boundary formation is the motion of GNDs, as opposed to (for example) inhomogeneous flows of SSDs.

There still remain many fascinating mesoscale experiments, such as dislocation avalanches (Miguel et al., 2001; Dimiduk et al., 2006), size-dependent hardness (smaller is stronger) (Uchic et al., 2004), and complex anisotropic loading (Schmitt et al., 1991; Lopes et al., 2003), that we hope to emulate. We intend in the future to include several relevant additional ingredients to our dynamics, such as vacancies (C.1), impurities (C.2), immobile dislocations/SSDs and slip systems, to reflect real materials.

Acknowledgments

Appendix A. Physical quantities in terms of the plastic distortion tensor β^{p}

In an isotropic infinitely large medium, the local deformation $\boldsymbol{u}$, the elastic distortion β^{e} and the internal long-range stress σ^{int} can be expressed (Mura, 1991; Limkumnerd and Sethna, 2006) in terms of the plastic distortion field β^{p} in Fourier space:

$$\widetilde{\boldsymbol{u}}_i(\mathbf{k}) = N_{ikl}(\mathbf{k})\widetilde{\beta}^{\mathrm{p}}_{kl}(\mathbf{k}),$$
$$N_{ikl}(\mathbf{k}) = -\frac{i}{k^2}(k_k\delta_{il}+k_l\delta_{ik}) - i\frac{vk_i\delta_{kl}}{(1-v)k^2} + i\frac{k_ik_kk_l}{(1-v)k^4}; \tag{A.1}$$

$$\widetilde{\beta}^{\mathrm{e}}_{ij}(\mathbf{k}) = T_{ijkl}(\mathbf{k})\widetilde{\beta}^{\mathrm{p}}_{kl}(\mathbf{k}),$$
$$T_{ijkl}(\mathbf{k}) = \frac{1}{k^2}(k_ik_k\delta_{jl}+k_ik_l\delta_{jk}-k^2\delta_{ik}\delta_{jl}) + \frac{k_ik_j}{(1-v)k^4}(vk^2\delta_{kl}-k_kk_l); \tag{A.2}$$

$$\widetilde{\sigma}^{\mathrm{int}}_{ij}(\mathbf{k}) = M_{ijmn}(\mathbf{k})\widetilde{\beta}^{\mathrm{p}}_{mn}(\mathbf{k}),$$
$$M_{ijmn}(\mathbf{k}) = \frac{2uv}{1-v}\left(\frac{k_mk_n\delta_{ij}+k_ik_j\delta_{mn}}{k^2}-\delta_{ij}\delta_{mn}\right) + u\left(\frac{k_ik_m}{k^2}\delta_{jn}+\frac{k_jk_n}{k^2}\delta_{im}-\delta_{im}\delta_{jn}\right)$$
$$+ u\left(\frac{k_fik_n}{k^2}\delta_{jm}+\frac{k_jk_m}{k^2}\delta_{in}-\delta_{in}\delta_{jm}\right) - \frac{2u}{1-v}\frac{k_ik_jk_mk_n}{k^4}. \tag{A.3}$$

All these expressions are valid for systems with periodic boundary conditions.

According to the definition Eq. (12) of the crystalline orientation Λ, we can replace ω^e with β^e and ϵ^e by using the elastic distortion tensor decomposition Eq. (A.2)

$$\Lambda_i = \frac{1}{2}\varepsilon_{ijk}(\beta_{jk}^e - \epsilon_{jk}^e). \tag{A.4}$$

Here the permutation factor acting on the symmetric elastic strain tensor gives zero. Hence we can express the crystalline orientation vector Λ in terms of β^p by using Eq. (A.2)

$$
\begin{aligned}
\widetilde{\Lambda}_i(\mathbf{k}) &= \frac{1}{2}\varepsilon_{ijk}\left\{\frac{1}{k^2}(k_jk_s\delta_{kt} + k_jk_t\delta_{ks} - k^2\delta_{js}\delta_{kt}) + \frac{k_jk_k}{(1-v)k^4}(vk^2\delta_{st} - k_sk_t)\right\}\widetilde{\beta}_{st}^p(\mathbf{k}) \\
&= \frac{1}{2k^2}(\varepsilon_{ijt}k_jk_s + \varepsilon_{ijs}k_jk_t - k^2\varepsilon_{ist})\widetilde{\beta}_{st}^p(\mathbf{k}).
\end{aligned}
\tag{A.5}
$$

Appendix B. Energy dissipation rate

B.1. Free energy in Fourier space

In the absence of external stress, the free energy $\mathcal{F}$ is the elastic energy caused by the internal long-range stress

$$\mathcal{F} = \int d^3\mathbf{x}\, \frac{1}{2}\sigma_{ij}^{int}\epsilon_{ij}^e = \int d^3\mathbf{x}\, \frac{1}{2}C_{ijmn}\epsilon_{ij}^e\epsilon_{mn}^e, \tag{B.1}$$

where the stress is $\sigma_{ij}^{int} = C_{ijmn}\epsilon_{mn}^e$, with C_{ijmn} the stiffness tensor.

Using the symmetry of C_{ijmn} and ignoring large rotations, $\epsilon_{ij}^e = (\beta_{ij}^e + \beta_{ji}^e)/2$, we can rewrite the elastic energy $\mathcal{F}$ in terms of β^e

$$\mathcal{F} = \int d^3\mathbf{x}\, \frac{1}{2}C_{ijmn}\beta_{ij}^e\beta_{mn}^e. \tag{B.2}$$

Performing a Fourier transform on both β_{ij}^p and β_{mn}^p simultaneously gives

$$\mathcal{F} = \int d^3\mathbf{x} \int \frac{d^3\mathbf{k}}{(2\pi)^3} \int \frac{d^3\mathbf{k}'}{(2\pi)^3}\, e^{i(\mathbf{k}+\mathbf{k}')\mathbf{x}}\left(\frac{1}{2}C_{ijmn}\widetilde{\beta}_{ij}^e(\mathbf{k})\widetilde{\beta}_{mn}^e(\mathbf{k}')\right). \tag{B.3}$$

Integrating out the spatial variable $\mathbf{x}$ leaves a $\delta-$function $\delta(\mathbf{k}+\mathbf{k}')$ in Eq. (B.3). We hence integrate out the k-space variable $\mathbf{k}'$

$$\mathcal{F} = \int \frac{d^3\mathbf{k}}{(2\pi)^3}\, \frac{1}{2}C_{ijmn}\widetilde{\beta}_{ij}^e(\mathbf{k})\widetilde{\beta}_{mn}^e(-\mathbf{k}). \tag{B.4}$$

Substituting Eq. (A.2) into Eq. (B.4) gives

$$\mathcal{F} = \int \frac{d^3\mathbf{k}}{(2\pi)^3}\, \frac{1}{2}\left(C_{ijmn}T_{ijpq}(\mathbf{k})T_{mnst}(-\mathbf{k})\right)\widetilde{\beta}_{pq}^p(\mathbf{k})\widetilde{\beta}_{st}^p(-\mathbf{k}) = -\int \frac{d^3\mathbf{k}}{(2\pi)^3}\, \frac{1}{2}M_{pqst}(\mathbf{k})\widetilde{\beta}_{pq}^p(\mathbf{k})\widetilde{\beta}_{st}^p(-\mathbf{k}), \tag{B.5}$$

where we skip straightforward but tedious simplifications.

When turning on the external stress, we repeat the same procedure used in Eq. (B.3), yielding

$$\mathcal{F}^{ext} = -\int d^3\mathbf{x}\, \sigma_{ij}^{ext}\beta_{ij}^p = -\int \frac{d^3\mathbf{k}}{(2\pi)^3}\, \widetilde{\sigma}_{ij}^{ext}(\mathbf{k})\widetilde{\beta}_{ij}^p(-\mathbf{k}). \tag{B.6}$$

B.2. Calculation of energy functional derivative with respect to the GND density ϱ

According to Eq. (17), the infinitesimal change of the variable $\delta\varrho$ is given in terms of $\delta\beta^p$

$$\delta\varrho_{ijk} = -g_{ijls}\partial_l(\delta\beta_{sk}^p). \tag{B.7}$$

Substituting Eq. (B.7) into Eq. (27) and applying integration by parts, the infinitesimal change of $\mathcal{F}$ is hence rewritten in terms of β^p

$$\delta\mathcal{F}[\beta^p] = \int d^3\mathbf{x}\, g_{ijls}\partial_l\left(\frac{\delta\mathcal{F}}{\delta\varrho_{ijk}}\right)\delta\beta_{sk}^p. \tag{B.8}$$

According to Eq. (24), it suggests

$$\delta\mathcal{F}[\beta^p] = \int d^3\mathbf{x}\, \frac{\delta\mathcal{F}}{\delta\beta^p_{sk}}\delta\beta^p_{sk} = \int d^3\mathbf{x}\,(-\sigma_{sk})\delta\beta^p_{sk}. \tag{B.9}$$

Comparing Eq. (B.8) and Eq. (B.9) implies

$$g_{ijls}\partial_l\left(\frac{\delta\mathcal{F}}{\delta\varrho_{ijk}}\right) = -\sigma_{sk}, \tag{B.10}$$

up to a total derivative which we ignore due to the use of periodic boundary conditions.

B.3. Derivation of energy dissipation rate

We can apply variational methods to calculate the dissipation rate of the free energy. As is well known, the general elastic energy $\mathcal{E}$ in a crystal can be expressed as $\mathcal{E} = \frac{1}{2}\int d^3\mathbf{x}\,\sigma_{ij}\epsilon^e_{ij}$, with ϵ^e_{ij} the elastic strain. An infinitesimal change of $\mathcal{E}$ is:

$$\delta\mathcal{E} = \frac{1}{2}\int d^3\mathbf{x}\,\sigma_{ij}\delta\epsilon^e_{ij} + \frac{1}{2}\int d^3\mathbf{x}\,\delta\sigma_{ij}\epsilon^e_{ij} = \int d^3\mathbf{x}\,\sigma_{ij}\delta\epsilon^e_{ij}, \tag{B.11}$$

where we use $\sigma_{ij}\delta\epsilon^e_{ij} = C_{ijkl}\epsilon^e_{kl}\delta\epsilon^e_{ij} = \delta\sigma_{ij}\epsilon^e_{ij}$.

So the infinitesimal change of the free energy Eq. (20) is

$$\delta\mathcal{F} = \int d^3\mathbf{x}\left(\sigma^{int}_{ij}\delta\epsilon^e_{ij} - \sigma^{ext}_{ij}\delta\epsilon^p_{ij}\right). \tag{B.12}$$

We apply the relation $\epsilon^e = \epsilon - \epsilon^p$, where ϵ^p is the plastic strain and ϵ is the total strain:

$$\delta\mathcal{F} = \int d^3\mathbf{x}\left(\sigma^{int}_{ij}\delta\epsilon_{ij} - \sigma^{int}_{ij}\delta\epsilon^p_{ij} - \sigma^{ext}_{ij}\delta\epsilon^p\right). \tag{B.13}$$

Using the symmetry of σ_{ij} and ignoring large rotations, $\epsilon_{ij} = \frac{1}{2}(\partial_i u_j + \partial_j u_i)$, we can rewrite the first term of Eq. (B.13) as $\int d^3\mathbf{x}\,\sigma^{int}_{ij}\delta(\partial_i u_j)$. Integrating by parts yields $\int d^3\mathbf{x}\left(\partial_i(\delta u_j\sigma^{int}_{ij}) - \delta u_j\partial_i\sigma^{int}_{ij}\right)$. We can convert the first volume integral to a surface integral, which vanishes for an infinitely large system. Hence

$$\delta\mathcal{F} = \int d^3\mathbf{x}\left(\partial_i\sigma^{int}_{ij}\delta u_j - (\sigma^{int}_{ij} + \sigma^{ext}_{ij})\delta\epsilon^p_{ij}\right). \tag{B.14}$$

The first term of Eq. (B.14) is zero assuming instantaneous elastic relaxation due to the local force equilibrium condition,

$$\delta\mathcal{F} = -\int d^3\mathbf{x}\,(\sigma^{int}_{ij} + \sigma^{ext}_{ij})\delta\beta^p_{ij}, \tag{B.15}$$

using the symmetry of σ_{ij} and $\epsilon^p_{ij} = \frac{1}{2}(\beta^p_{ij} + \beta^p_{ji})$.

The free energy dissipation rate is thus $\delta\mathcal{F}/\delta t$ for $\delta\beta^p_{ij} = \frac{\partial\beta^p}{\partial t}\delta t$, hence

$$\frac{\partial\mathcal{F}}{\partial t} = -\int d^3\mathbf{x}\,(\sigma^{int}_{ij} + \sigma^{ext}_{ij})\frac{\partial\beta^p_{ij}}{\partial t} = -\int d^3\mathbf{x}\,(\sigma^{int}_{ij} + \sigma^{ext}_{ij})J_{ij}. \tag{B.16}$$

When dislocations are allowed to climb, substituting the CGD current Eq. (36) into Eq. (B.16) implies that the free energy dissipation rate is strictly negative

$$\frac{\partial\mathcal{F}}{\partial t} = -\int d^3\mathbf{x}\,(\sigma^{int}_{ij} + \sigma^{ext}_{ij})\left[v_l\varrho_{lij}\right] = -\int d^3\mathbf{x}\,\frac{|\varrho|}{D}v^2 \leqslant 0. \tag{B.17}$$

When removing dislocation climb by considering the mobile dislocation population, we substitute Eq. (40) into Eq. (B.16) to guarantee that the rate of the change of the free energy density is also the negative of a perfect square

$$\frac{\partial\mathcal{F}}{\partial t} = -\int d^3\mathbf{x}(\sigma^{int}_{ij} + \sigma^{ext}_{ij})\left[v'_l\left(\varrho_{lij} - \frac{1}{3}\delta_{ij}\varrho_{lkk}\right)\right] = -\int d^3\mathbf{x}\,\frac{|\varrho|}{D}v'^2 \leqslant 0. \tag{B.18}$$

Appendix C. Model Extensions: Adding vacancies and disorder to CDD

C.1. Coupling vacancy diffusion to CDD

In plastically deformed crystals at low temperature, dislocations usually move only in the glide plane because vacancy diffusion is almost frozen out. When temperature increases, vacancy diffusion leads to dislocation climb out of the glide plane. At intermediate temperatures, slow vacancy diffusion can enable local creep. The resulting dynamics should couple

the vacancy and dislocation fields in non-trivial ways. Here we couple the vacancy diffusion to the dislocation motion in our CDD model.

We introduce an order parameter field $c(\mathbf{x})$, indicating the vacancy concentration density at the point $\mathbf{x}$. The free energy $\mathcal{F}$ is thus expressed

$$\mathcal{F} = \mathcal{F}^{Dis} + \mathcal{F}^{Vac} = \int d^3\mathbf{x}\left(\frac{1}{2}\sigma_{ij}\epsilon_{ij}^{e} + \frac{1}{2}\alpha(c - c_0)^2\right), \tag{C.1}$$

where α is a positive material parameter related to the vacancy creation energy, and c_0 is the overall equilibrium vacancy concentration density.

Assuming that GNDs share the velocity $\boldsymbol{v}$ in an infinitesimal volume, we write the current J for GNDs

$$J_{ij} = v_u \varrho_{uij}. \tag{C.2}$$

The current trace J_{ii} describes the rate of volume change, which acts as a source and sink of vacancies. The coupling dynamics for vacancies is thus given as

$$\partial_t c = \gamma\nabla^2 c + J_{ii}, \tag{C.3}$$

where γ is a positive vacancy diffusion constant.

The infinitesimal change of the free energy $\mathcal{F}$ (Eq. C.1) is

$$\delta\mathcal{F} = \int d^3\mathbf{x}\left(\frac{\delta\mathcal{F}^{Dis}}{\delta\beta_{ij}^{p}}\delta\beta_{ij}^{p} + \frac{\delta\mathcal{F}^{Vac}}{\delta c}\delta c\right). \tag{C.4}$$

We apply Eq. (B.15) and $\delta\mathcal{F}^{Vac}/\delta c = \alpha(c - c_0)$

$$\delta\mathcal{F} = \int d^3\mathbf{x}\left(-\sigma_{ij}\delta\beta_{ij}^{p} + \alpha(c - c_0)\delta c\right). \tag{C.5}$$

The free energy dissipation rate is thus $\delta\mathcal{F}/\delta t$ for $\delta\beta_{ij}^{p} = \frac{\partial\beta^{p}}{\partial t}\delta t$ and $\delta c = \frac{\partial c}{\partial t}\delta c$, hence

$$\frac{\partial\mathcal{F}}{\partial t} = -\int d^3\mathbf{x}\left(\sigma_{ij}\frac{\partial\beta_{ij}^{p}}{\partial t} - \alpha(c - c_0)\frac{\partial c}{\partial t}\right). \tag{C.6}$$

Substituting the current J (Eq. C.2) and and Eq. (C.3) into Eq. (C.6) gives

$$\frac{\partial\mathcal{F}}{\partial t} = -\int d^3\mathbf{x}\left(\sigma_{ij}(v_u\varrho_{uij}) - \alpha(c - c_0)(\gamma\nabla^2 c + v_u\varrho_{uii})\right) = -\int d^3\mathbf{x}\left((\sigma_{ij} - \alpha(c - c_0)\delta_{ij})\varrho_{uij}\right)v_u - \int d^3\mathbf{x}\alpha\gamma(\nabla c)^2, \tag{C.7}$$

where we integrate by parts by assuming an infinitely large system.

If we choose the velocity $v_u = \frac{D}{|\varrho|}(\sigma_{ij} - \alpha(c - c_0)\delta_{ij})\varrho_{uij}$, ($D$ is a positive material dependent constant and $1/|\varrho|$ is added for the same reasons as discussed in Section 2.3.1), the free energy is guaranteed to decrease monotonically. The coupling dynamics for both GNDs and vacancies is thus

$$\begin{cases} \partial_t\beta_{ij}^{p} = \frac{D}{|\varrho|}(\sigma_{mn} - \alpha(c - c_0)\delta_{mn})\varrho_{umn}\varrho_{uij}, \\ \partial_t c = \gamma\nabla^2 c + \frac{D}{|\varrho|}(\sigma_{mn} - \alpha(c - c_0)\delta_{mn})\varrho_{umn}\varrho_{ukk}. \end{cases} \tag{C.8}$$

This dynamics gives us a clear picture of the underlying physical mechanism: the vacancies contribute an extra hydrostatic pressure $p = -\alpha(c - c_0)$.

C.2. Coupling disorder to CDD

In real crystals, the presence of precipitates or impurities results in a force pinning nearby dislocations. We can mimic this effect by incorporating a spatially varying random potential field $V(\mathbf{x})$. In our CDD model, we can add the interaction energy between GNDs and random disorder into the free energy $\mathcal{F}$ (Eq. (C.6))

$$\mathcal{F} = \mathcal{F}_E + \mathcal{F}_I = \int d^3\mathbf{x}\left(\frac{1}{2}\sigma_{ij}^{int}\epsilon_{ij}^{e} - \sigma_{ij}^{ext}\epsilon_{ij}^{p} + V(\mathbf{x})|\varrho|\right), \tag{C.9}$$

where $\mathcal{F}_E$ indicates the elastic free energy corresponding to the integral of the first two terms, and $\mathcal{F}_I$ indicates the interaction energy, the integral of the last term.

An infinitesimal change of the free energy is written

$$\delta\mathcal{F} = \delta\mathcal{F}_E + \delta\mathcal{F}_I = \int d^3\mathbf{x}\left(\frac{\delta\mathcal{F}_E}{\delta\beta_{ij}^{p}}\delta\beta_{ij}^{p} + \frac{\delta\mathcal{F}_I}{\delta\beta_{sk}^{p}}\delta\beta_{sk}^{p}\right). \tag{C.10}$$

In an infinitely large system, Eq. (B.15) gives

$$\frac{\delta\mathcal{F}_E}{\delta\beta_{ij}^{p}} = -(\sigma_{ij}^{int} + \sigma_{ij}^{ext}), \tag{C.11}$$

and Eq. (B.8) implies

$$\delta\mathcal{F}_I = \int d^3\mathbf{x} g_{ijls}\partial_l\left(\frac{\delta\mathcal{F}_I}{\delta\varrho_{ijk}}\right)\delta\beta_{sk}^{p} = \int d^3\mathbf{x} g_{ijls}\partial_l\left(V(\mathbf{x})\frac{\varrho_{ijk}}{|\varrho|}\right)\delta\beta_{sk}^{p}. \tag{C.12}$$

Substituting Eq. (C.11) and Eq. (C.12) into Eq. (C.10) gives

$$\delta\mathcal{F} = -\int d^3\mathbf{x}\left(\sigma_{ij}^{int} + \sigma_{ij}^{ext} - g_{mnli}\partial_l\left(V(\mathbf{x})\frac{\varrho_{mnj}}{|\varrho|}\right)\right)\delta\beta_{ij}^{p} = -\int d^3\mathbf{x}\sigma_{ij}^{eff}\delta\beta_{ij}^{p}, \tag{C.13}$$

where the effective stress field is $\sigma_{ij}^{eff} = \sigma_{ij}^{int} + \sigma_{ij}^{ext} - g_{mnli}\partial_l\left(V(\mathbf{x})\frac{\varrho_{mnj}}{|\varrho|}\right)$.

By replacing σ_{ij} with σ_{ij}^{eff} in the equation of motion of either allowing climb (Eq. 36) or removing climb (Eqs. 40 and 44), we achieve the new CDD model that models GNDs interacting with disorder.

Appendix D. Details of the Simulations

D.1. Finite size effects

Although we suspect that our simulations don't have weak solutions (Choi et al., in preparation), we can show that these solutions converge statistically. We use two ways to exhibit the statistical convergence.

When we continue to decrease the grid spacing to zero (the continuum limit), we show the statistical convergence of correlation functions of ρ, Λ, and $\beta^{p,l}$, with a slow expected drift of apparent exponents with system size, see Fig. C.13.

We can also decrease the initial correlated length scales in a large two dimensional simulation. Since the emergent self-similar structures are always developed below the initial correlated lengths, as discussed in Section 4.2, this is similar to decreasing the system size by reducing the initial correlated lengths. In Fig. C.14, the correlation functions of ρ, Λ, and $\beta^{p,l}$ collapse into a single scaling curve, using finite size scaling.

D.2. Gaussian random initial conditions

Gaussian random fields are extensively used in physical modelings to mimic stochastic fluctuations with a correlated length scale. In our simulations, we construct an initially random plastic distortion, a nine-component tensor field, where every component is an independent Gaussian random field sharing a underlying length scale.
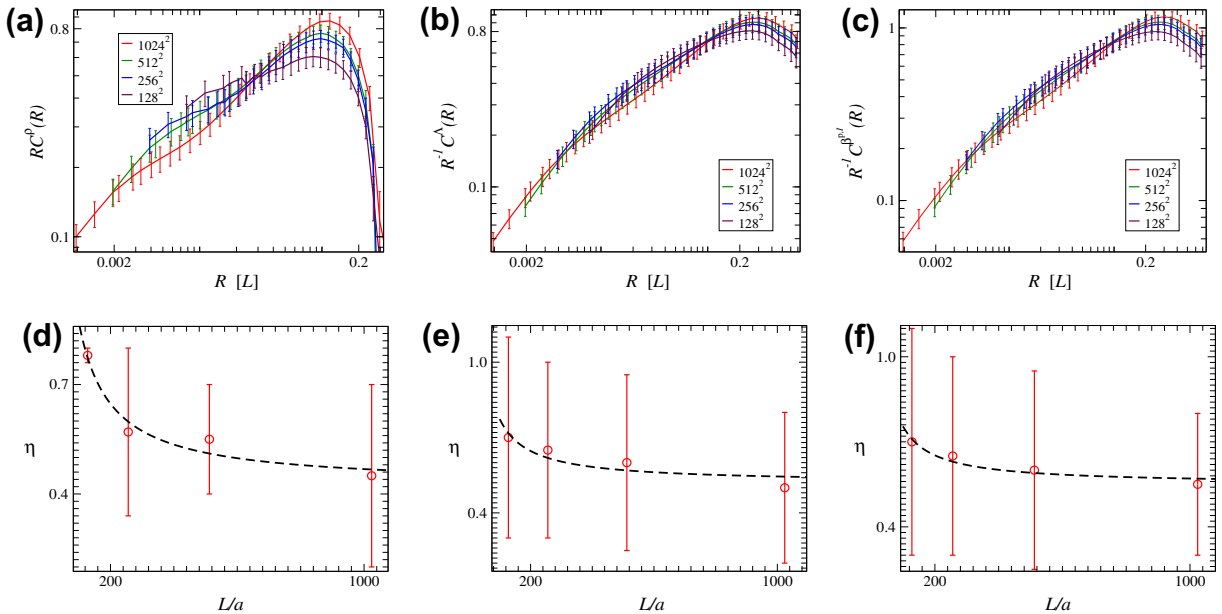
Fig. C.13. Statistical convergence of correlation functions of Λ, ρ and $\beta^{p,l}$ by varying lattice sizes in two dimensions. We compare correlation functions of relaxed glide-only states (GOD-MDP) at resolutions from 128^2 to 1024^2 systems. *Top:* We see that the correlation functions in all cases exhibit similar power laws in (a)–(c); *Bottom:* (d)–(f) show a single underlying critical exponent which appears to converge with increasing resolution, where a is the grid spacing. The black dashed lines are guides to the eye.
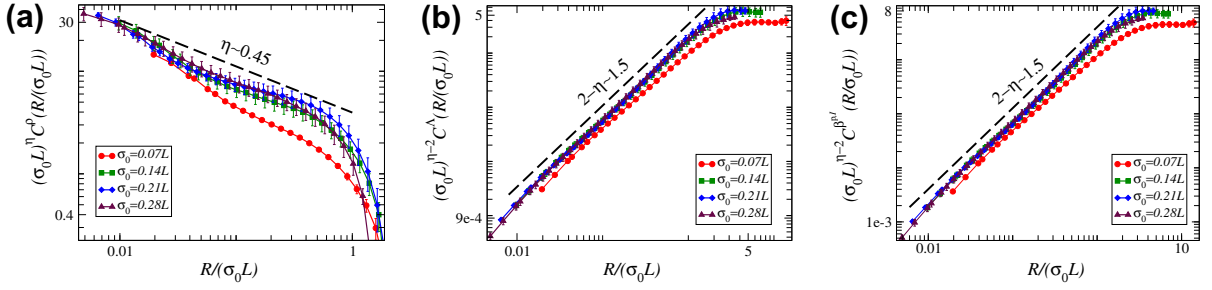
Fig. C.14. Statistical convergence of correlation functions of Λ, ρ and $\beta^{p,I}$ by varying the initial length scales in 1024^2 simulations. We measure correlation functions of relaxed glide-only states (GOD-MDP) at initial correlated lengths from $0.07L$ to $0.28L$. In (a)–(c), the radial-length variable R is rescaled by their initial correlation lengths, and the corresponding correlation functions are divided by the same lengths to the exhibiting powers. They roughly collapse into the scaling laws. Notice that the power laws measured in the state with the initial correlated length $0.07L$ get distorted due to the small outer cutoff.

We define a Gaussian random field f with correlation length σ_0 by convolving white noise $\langle\xi(\mathbf{x})\xi(\mathbf{x}')\rangle = \delta(\mathbf{x}-\mathbf{x}')$ with a Gaussian of width σ_0:

$$f(\mathbf{x}) = \int d^3\mathbf{x}'\,\xi(\mathbf{x}')e^{-(\mathbf{x}-\mathbf{x}')^2/\sigma_0^2}. \tag{D.1}$$

In Fourier space, this can be done as a multiplication:

$$\widetilde{f}(\mathbf{k}) = e^{-\sigma_0^2 k^2/4}\widetilde{\xi}(\mathbf{k}). \tag{D.2}$$

The square $\widetilde{f}(\mathbf{k})\widetilde{f}(-\mathbf{k}) = e^{-\sigma_0^2 k^2/2}$ implies that the correlation function $\langle f(\mathbf{x})f(\mathbf{x}')\rangle = (2\pi\sigma_0^2)^{-3/2}e^{-(\mathbf{x}-\mathbf{x}')^2/(2\sigma_0^2)}$.

In our simulations, the initial plastic distortion tensor field β^p is constructed in Fourier space

$$\widetilde{\beta}_{ij}^p(\mathbf{k}) = e^{-\sigma_0^2 k^2/4}\widetilde{\zeta}_{ij}(\mathbf{k}), \tag{D.3}$$

where the white noise signal ζ is characterized as $\langle\zeta_{(i,j)}(\mathbf{x})\zeta_{(i,j)}(\mathbf{x}')\rangle = A_{(i,j)}\delta(\mathbf{x}-\mathbf{x}')$, and in Fourier space $\frac{1}{V}\widetilde{\zeta}_{(i,j)}(\mathbf{k})\widetilde{\zeta}_{(i,j)}(-\mathbf{k}) = A_{(i,j)}$. (We use (i,j) to indicate a component of the tensor field, to avoid the Einstein summation rule.) The correlation function of each component of $\beta^{p,I}$ is thus expressed in Fourier space

$$\widetilde{C}_{(i,j)}^{\beta^{p,I}} = 2\langle\beta_{(i,j)}^{p,I}\beta_{(i,j)}^{p,I}\rangle(2\pi)^3\delta(\mathbf{k}) - \frac{2}{V}\widetilde{\beta}_{(i,j)}^p(\mathbf{k})\widetilde{\beta}_{(i,j)}^p(-\mathbf{k}) = 2\langle\beta_{(i,j)}^{p,I}\beta_{(i,j)}^{p,I}\rangle(2\pi)^3\delta(\mathbf{k}) - 2A_{(i,j)}e^{-\sigma_0^2 k^2/2}, \tag{D.4}$$

where the Gaussian kernel width σ_0, as a standard length scale, defines the correlation length of our simulation. (In our earlier work, we use a non-standard definition for the correlation length, so our σ_0 equals the old length scale times $\sqrt{2}$.)

According to Eq. (9) and Eq. (D.3), we can express the initial GND density field ρ in Fourier space

$$\widetilde{\rho}_{ij}(\mathbf{k}) = -i\varepsilon_{ilm}e^{-\sigma_0^2 k^2/4}k_l\widetilde{\zeta}_{mj}(\mathbf{k}). \tag{D.5}$$

The scalar invariant $\mathcal{C}_{tot}^\rho$ of the correlation function of ρ is thus expressed in Fourier space

$$\mathcal{C}_{tot}^\rho(\mathbf{k}) = \frac{1}{V}\widetilde{\rho}_{ij}(\mathbf{k})\widetilde{\rho}_{ij}(-\mathbf{k}) = \frac{1}{V}e^{-\sigma_0^2 k^2/2}\left(k^2\delta_{mn} - k_m k_n\right)\widetilde{\zeta}_{mj}(\mathbf{k})\widetilde{\zeta}_{nj}(-\mathbf{k}). \tag{D.6}$$

The resulting initial GND density is not Gaussian correlated, unlike the initial plastic distortion. Fig. D.15 exhibits the initial GND density map due to the Gaussian random plastic distortions with the correlation length $0.28L$, and its correlation function. We compare the latter to the correlation functions of both a sinusoidal wave and a single periodic superposition of Gaussian peaks. The similarity of the three curves shows that our Gaussian random initial condition at $\sigma_0 \sim 0.28L$ approaches the largest effective correlation length possible for periodic boundary conditions.

Appendix E. Other correlation functions unrelated to static scaling theory

E.1. Correlation functions of the strain-history-dependent plastic deformation and distortion fields

The curl-free strain-history-dependent part of the plastic distortion field, as shown in Fig. D.16(a), (c), and (e), exhibits structures reminiscent of self-similar morphology. We correlate their differences at neighboring points
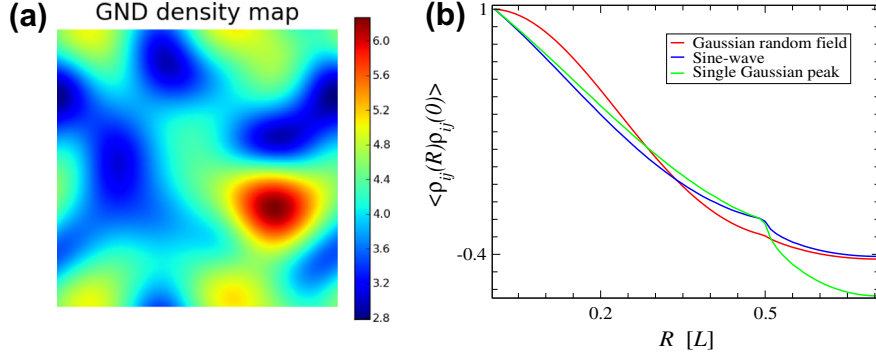
Fig. D.15. Gaussian random initial conditions with the correlated length scale $0.28L$ in two dimensions. (a) shows the initial net GND density map; (b) exhibits the correlation functions of ρ under various initial conditions, where we compare the Gaussian random field to both a sinusoidal wave and a single periodic superposition of Gaussian peaks. The kink arises due to the edges and corners of the square unit cell.

$$\mathcal{C}_{tot}^{\beta^{p,H}}(\mathbf{x}) = \langle((\beta_{ij}^{p,H}(\mathbf{x}) - \beta_{ij}^{p,H}(\mathbf{0}))(\beta_{ij}^{p,H}(\mathbf{x}) - \beta_{ij}^{p,H}(\mathbf{0}))\rangle, \tag{E.1}$$

$$\mathcal{C}_{per}^{\beta^{p,H}}(\mathbf{x}) = \langle((\beta_{ij}^{p,H}(\mathbf{x}) - \beta_{ij}^{p,H}(\mathbf{0}))(\beta_{ji}^{p,H}(\mathbf{x}) - \beta_{ji}^{p,H}(\mathbf{0}))\rangle, \tag{E.2}$$

$$\mathcal{C}_{tr}^{\beta^{p,H}}(\mathbf{x}) = \langle((\beta_{ii}^{p,H}(\mathbf{x}) - \beta_{ii}^{p,H}(\mathbf{0}))(\beta_{jj}^{p,H}(\mathbf{x}) - \beta_{jj}^{p,H}(\mathbf{0}))\rangle. \tag{E.3}$$

Consider also the deformation field ψ (shown in Fig. D.16 of Eq. (19)) whose gradient gives the strain-history-dependent plastic deformation $\beta^{p,H}$. Similarly to the crystalline orientation Λ, we correlate differences of ψ. The unique rotational invariant of its two-point correlation functions is written

$$\mathcal{C}^{\psi}(\mathbf{x}) = 2\langle\psi^2\rangle - 2\langle\psi_i(\mathbf{x})\psi_i(\mathbf{0})\rangle. \tag{E.4}$$

In Fig. D.17, the correlation functions of the strain-history-dependent plastic distortion $\beta^{p,H}$ in both 1024^2 and 128^3 simulations show critical exponents τ and τ'. Although apparently unrelated to the previous underlying critical exponent η, this exponents τ and τ' quantify the fractality of the strain-history-dependent plastic distortion. Fig. D.18 shows the correlation functions of the strain-history-dependent deformation ψ, with the critical exponent τ'' close to 2, which implies a smooth non-fractal field, shown in Fig. D.16(c) and (d). All measured critical exponents are listed in Table D.2.

Fig. D.17 shows the power-law dependence of the rotational invariants $\mathcal{C}_{per}^{\beta^{p,H}}$ and $\mathcal{C}_{tr}^{\beta^{p,H}}$ (they overlap). According to the definition $\widetilde{\beta}_{ij}^{p,H} = ik_i\widetilde{\psi}_j$, we can write down the Fourier-transformed forms of Eq. (E.2) and Eq. (E.3) respectively

$$\widetilde{\mathcal{C}}_{per}^{\beta^{p,H}}(\mathbf{k}) = 2\langle\beta_{ij}^{p,H}\beta_{ji}^{p,H}\rangle(2\pi)^3\delta(\mathbf{k}) - \frac{2}{V}k_ik_j\widetilde{\psi}_j(\mathbf{k})\widetilde{\psi}_i(-\mathbf{k}), \tag{E.5}$$

$$\widetilde{\mathcal{C}}_{tr}^{\beta^{p,H}}(\mathbf{k}) = 2\langle\beta_{ii}^{p,H}\beta_{jj}^{p,H}\rangle(2\pi)^3\delta(\mathbf{k}) - \frac{2}{V}k_ik_j\widetilde{\psi}_i(\mathbf{k})\widetilde{\psi}_j(-\mathbf{k}). \tag{E.6}$$

Except the zero-wavelength terms, the same functional forms shared by these two rotational scalars explain the observed overlapping power laws.

E.2. Stress–stress correlation functions

As the system relaxes to its final stress-free state, we can measure the fluctuations of the internal elastic stress fields, using a complete set of two rotational invariants of correlation functions (Fig. E.19(a,b)):

$$\mathcal{C}_{tot}^{\sigma}(\mathbf{x}) = \langle\sigma_{ij}^{int}(\mathbf{x})\sigma_{ij}^{int}(\mathbf{0})\rangle, \tag{E.7}$$

$$\mathcal{C}_{tr}^{\sigma}(\mathbf{x}) = \langle\sigma_{ii}^{int}(\mathbf{x})\sigma_{jj}^{int}(\mathbf{0})\rangle; \tag{E.8}$$

and in Fourier space

$$\widetilde{\mathcal{C}}_{tot}^{\sigma}(\mathbf{k}) = \frac{1}{V}\widetilde{\sigma}_{ij}^{int}(\mathbf{k})\widetilde{\sigma}_{ij}^{int}(-\mathbf{k}), \tag{E.9}$$

$$\widetilde{\mathcal{C}}_{tr}^{\sigma}(\mathbf{k}) = \frac{1}{V}\widetilde{\sigma}_{ii}^{int}(\mathbf{k})\widetilde{\sigma}_{jj}^{int}(-\mathbf{k}). \tag{E.10}$$

Because σ_{ij} is symmetric, these two correlation functions form a complete set of linear invariants under rotational transformations.
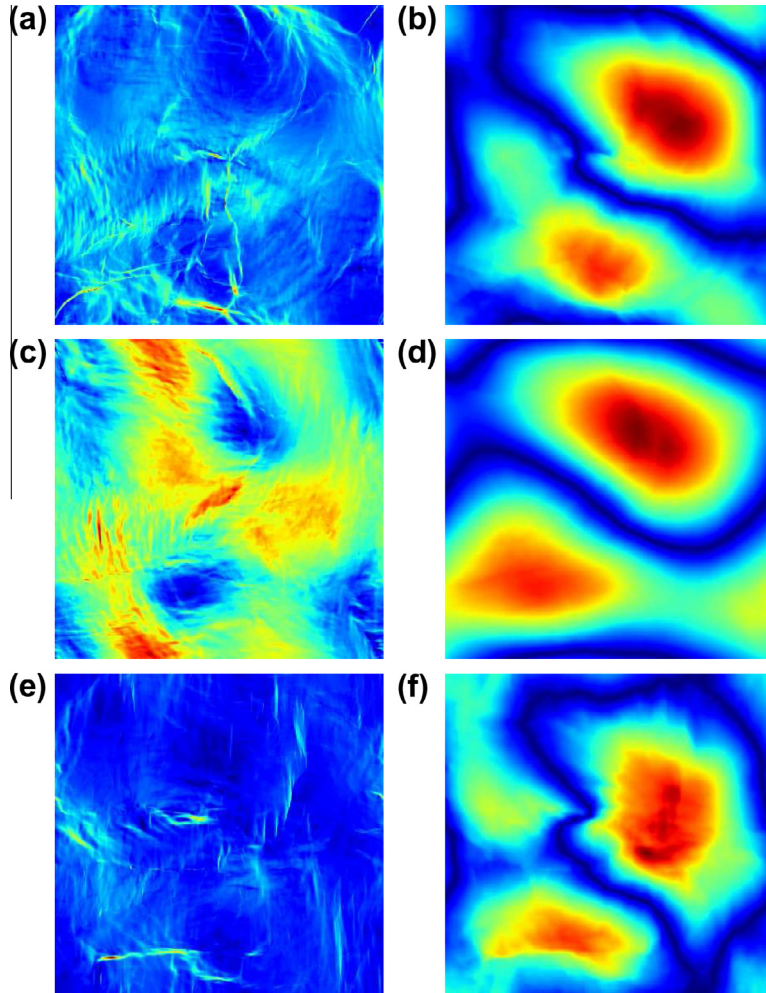
Fig. D.16. Strain-history-dependent fields $\beta^{p,H}$ and ψ in two dimensions for the relaxed states. *Top:* Dislocation climb is allowed; *Middle:* Glide-only using a mobile dislocation population; *Bottom:* Glide-only using a local vacancy pressure. *Left:* The strain-history-dependent plastic distortion $|\beta^{p,H}|$. (a), (c), and (e) exhibit patterns reminiscent of self-similar dislocation structures. *Right:* The strain-history-dependent plastic deformation $|\psi|$. (b), (d), and (f) exhibit smooth patterns with a little distortion, which are not fractal.
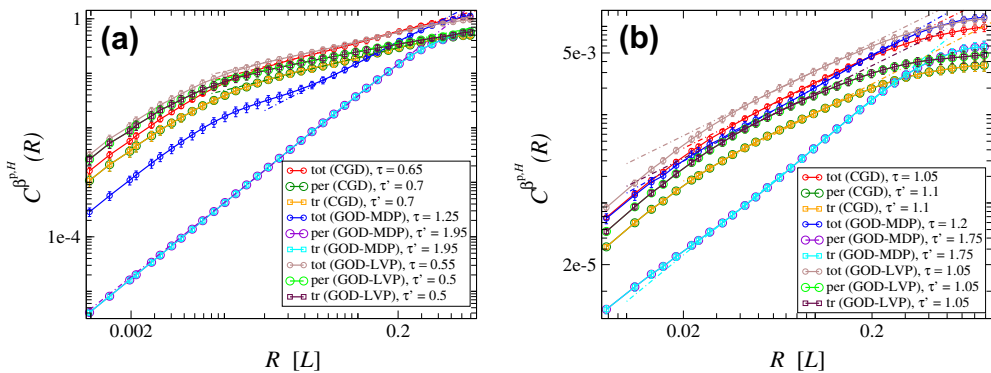
Fig. D.17. Correlation functions of $\beta^{p,H}$ in both two and three dimensions. In both (a) and (b), the correlation functions of the strain-history-dependent part of the plastic distortion $\beta^{p,H}$ are shown. *Left:* (a) is measured in relaxed, unstrained 1024^2 systems; *Right:* (b) is measured in relaxed, unstrained 128^3 systems. All dashed lines show estimated power laws quoted in Table D.2.
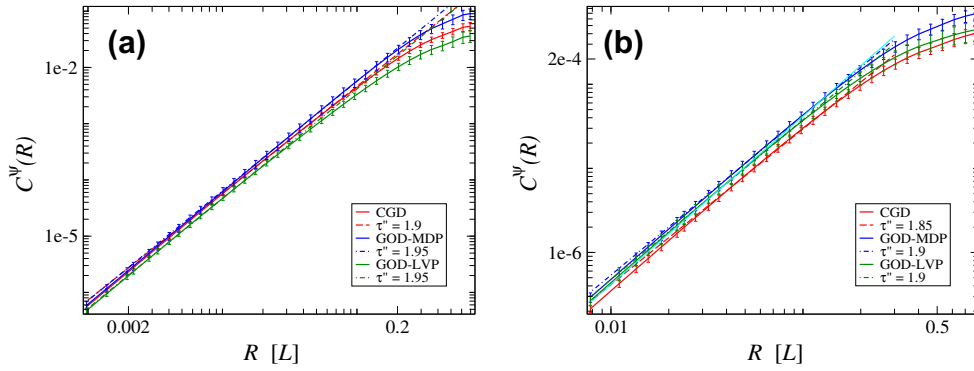
Fig. D.18. Correlation functions of ψ in both two and three dimensions. In (a) and (b), the correlation functions of the strain-history-dependent deformation ψ are shown. Red, blue, green lines indicate CGD, GOD-MDP, and GOD-LVP, respectively. *Left:* (a) is measured in relaxed, unstrained 1024^2 systems; *Right:* (b) is measured in relaxed, unstrained 128^3 systems. All dashed lines show estimated power laws quoted in Table D.2.

Table D.2
Critical exponents for correlation functions of strain-history-dependent fields at stress-free states. (C.F. and Exp. represent 'Correlation Functions' and 'Exponents', respectively.)

C.F.	S.T.	Simulations					
		Climb and glide		Glide only (MDP)		LVP glide only (LVP)	
		2D (1024^2)	3D (128^3)	2D (1024^2)	3D (128^3)	2D (1024^2)	3D (128^3)
$C_{tot}^{\beta^{p.H}}$	τ	0.65 ± 1.00	1.05 ± 0.65	1.25 ± 0.60	1.20 ± 0.50	0.55 ± 1.10	1.05 ± 0.65
$C_{per}^{\beta^{p.H}}$	τ'	0.70 ± 0.95	1.10 ± 0.60	1.95 ± 0.05	1.75 ± 0.15	0.50 ± 1.15	1.05 ± 0.70
$C_{tr}^{\beta^{p.H}}$	τ'	0.70 ± 0.95	1.10 ± 0.60	1.95 ± 0.05	1.75 ± 0.15	0.50 ± 1.15	1.05 ± 0.70
C^{ψ}	τ''	1.90 ± 0.10	1.85 ± 0.15	1.95 ± 0.05	1.90 ± 0.10	1.95 ± 0.05	1.90 ± 0.10

E.3. Energy density spectrum

The average internal elastic energy $\mathcal{E}$ is written

$$\mathcal{E} = \frac{1}{V} \int d^d \mathbf{x} \left[\frac{1}{2} \sigma_{ij}^{\text{int}} \epsilon_{ij}^{\text{e}} \right] = \frac{1}{V} \int d^d \mathbf{x} \frac{1}{4\mu} \left[\sigma_{ij}^{\text{int}} \sigma_{ij}^{\text{int}} - \frac{v}{1+v} \sigma_{ii}^{\text{int}} \sigma_{jj}^{\text{int}} \right], \tag{E.11}$$

where, in an isotropic bulk medium, the elastic strain ϵ^{e} is expressed in terms of σ^{int},

$$\epsilon_{ij}^{\text{e}} = \frac{1}{2\mu} \left(\sigma_{ij}^{\text{int}} - \frac{v}{1+v} \delta_{ij} \sigma_{kk}^{\text{int}} \right). \tag{E.12}$$

We can rewrite Eq. (E.11) in Fourier space

$$\mathcal{E} = \frac{1}{V} \int \frac{d^d \mathbf{k}}{(2\pi)^d} \frac{1}{4\mu} \left[\widetilde{\sigma}_{ij}^{\text{int}}(\mathbf{k}) \widetilde{\sigma}_{ij}^{\text{int}}(-\mathbf{k}) - \frac{v}{1+v} \widetilde{\sigma}_{ii}^{\text{int}}(\mathbf{k}) \widetilde{\sigma}_{jj}^{\text{int}}(-\mathbf{k}) \right]. \tag{E.13}$$

Substituting Eq. (E.9) and Eq. (E.10) into Eq. (E.13) gives

$$\mathcal{E} = \int \frac{d^d \mathbf{k}}{2^{d+2} \pi^d} \frac{1}{\mu} \left[\widetilde{\mathcal{C}}_{tot}^{\sigma}(\mathbf{k}) - \frac{v}{1+v} \widetilde{\mathcal{C}}_{tr}^{\sigma}(\mathbf{k}) \right] \tag{E.14}$$
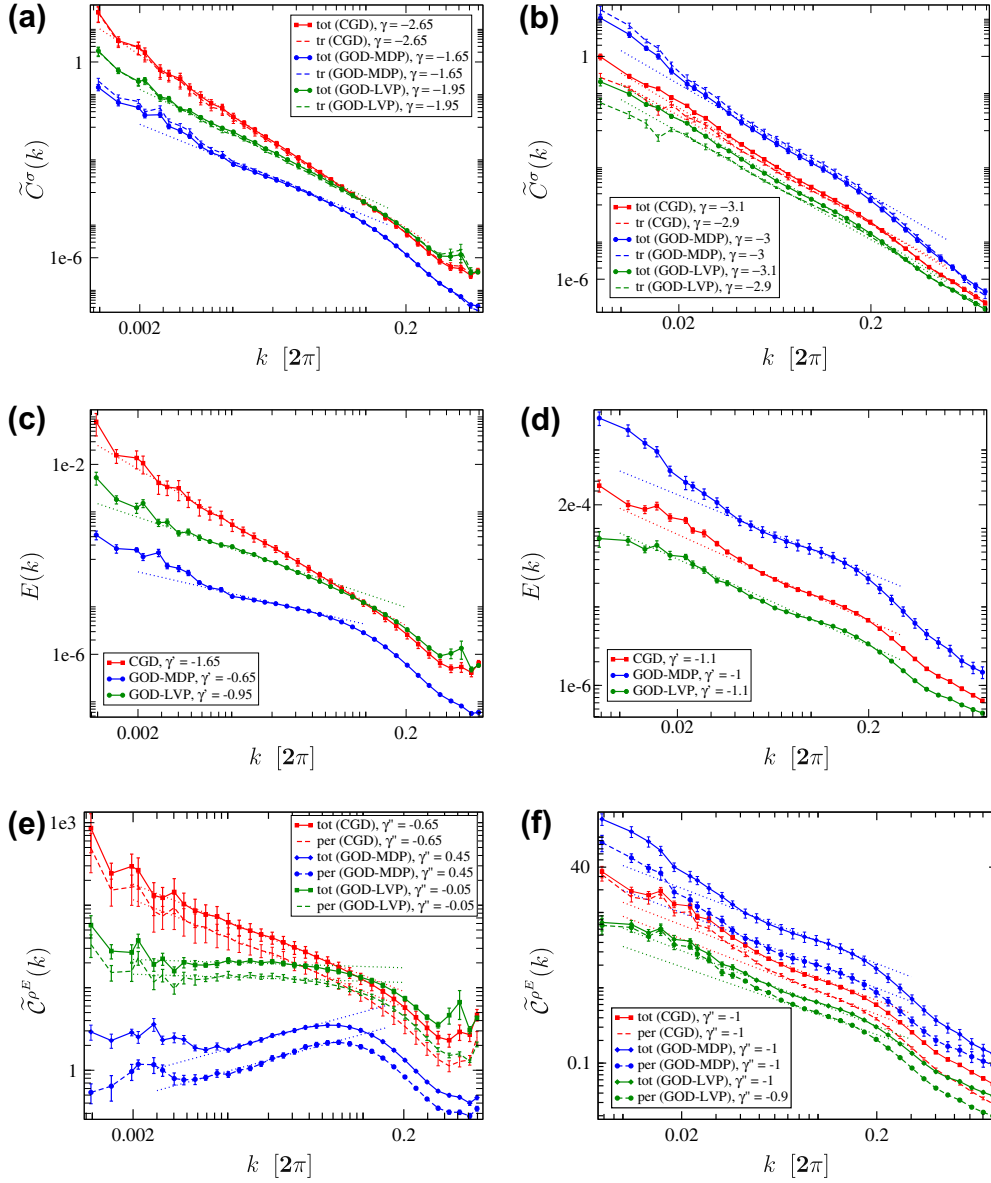
If the stress-stress correlation functions are isotropic, we can integrate out the angle variable of Eq. (E.14)

$$\mathcal{E} = \int_0^{\infty} dk \frac{f(d)}{\mu} k^{d-1} \left[\widetilde{\mathcal{C}}_{tot}^{\sigma}(k) - \frac{v}{1+v} \widetilde{\mathcal{C}}_{tr}^{\sigma}(k) \right], \tag{E.15}$$

where $f(d)$ is a constant function over the dimension d,

$$f(d) = \begin{cases} 1/(8\pi) & d = 2, \\ 1/(8\pi^2) & d = 3. \end{cases} \tag{E.16}$$

Fig. E.19. Stress-stress correlation functions $\widetilde{C}^\sigma(k)$, elastic energy spectrum $E(k)$, correlation functions of the stress-full part of GND density $\widetilde{C}^{\rho^E}(k)$. Red, blue, and green lines indicate CGD, GOD-MDP, and GOD-LVP, respectively. All dashed lines show estimated power laws quoted in Table E.3. (For interpretation of the references to color in this figure legend, the reader is referred to the web version of this article.)

Writing the elastic energy density in terms of the energy density spectrum $\mathcal{E}(t) = \int_0^\infty E(k,t)dk$ implies (Fig. E.19(c,d))

$$E(k) = \frac{f(d)}{\mu} k^{d-1} \left[\widetilde{C}^\sigma_{tot}(k) - \frac{v}{1+v} \widetilde{C}^\sigma_{tr}(k) \right]. \tag{E.17}$$

E.4. Correlation function of the stressful part of GND density

According to Eq. (14), the stressful part of GND density is defined as

$$\rho^E_{ij}(\mathbf{x}) = \varepsilon_{isl}\partial_s \epsilon^e_{lj}(\mathbf{x}). \tag{E.18}$$

Substituting Eq. (E.12) into Eq. (E.18) gives

$$\rho^E_{ij} = \frac{1}{2\mu}\varepsilon_{isl}\partial_s\left(\sigma^{int}_{lj} - \frac{v}{1+v}\delta_{lj}\sigma^{int}_{mm}\right). \tag{E.19}$$

The complete set of rotational invariants of the correlation function of ρ^E includes three scalar forms(Fig. E.19(e,f)):

$$\mathcal{C}^{\rho^E}_{tot}(\mathbf{x}) = \langle \rho^E_{ij}(\mathbf{x})\rho^E_{ij}(0)\rangle,$$ (E.20)

$$\mathcal{C}^{\rho^E}_{per}(\mathbf{x}) = \langle \rho^E_{ij}(\mathbf{x})\rho^E_{ji}(0)\rangle,$$ (E.21)

$$\mathcal{C}^{\rho^E}_{tr}(\mathbf{x}) = \langle \rho^E_{ii}(\mathbf{x})\rho^E_{jj}(0)\rangle,$$ (E.22)

where $\mathcal{C}^{\rho^E}_{tr}(\mathbf{x})$ is always zero due to $\rho^E_{ii} = 0$.

Substituting Eq. (E.19) into both Eqs. (E.20) and (E.21) and applying the Fourier transform gives

$$\widetilde{\mathcal{C}}^{\rho^E}_{tot}(\mathbf{k}) = \frac{1}{4\mu^2 V}\varepsilon_{isl}(ik_s)\left(\widetilde{\sigma}^{int}_{lj}(\mathbf{k}) - \frac{v}{1+v}\delta_{lj}\widetilde{\sigma}^{int}_{mm}(\mathbf{k})\right) \times \varepsilon_{ipq}(-ik_p)\left(\widetilde{\sigma}^{int}_{qj}(-\mathbf{k}) - \frac{v}{1+v}\delta_{qj}\widetilde{\sigma}^{int}_{nn}(-\mathbf{k})\right)$$

$$= \frac{k^2}{4\mu^2}\left(\frac{1}{V}\widetilde{\sigma}^{int}_{lj}(\mathbf{k})\widetilde{\sigma}^{int}_{lj}(-\mathbf{k})\right) - \frac{vk^2}{2\mu^2(1+v)^2}\left(\frac{1}{V}\widetilde{\sigma}^{int}_{mm}(\mathbf{k})\widetilde{\sigma}^{int}_{nn}(-\mathbf{k})\right),$$ (E.23)

$$\widetilde{\mathcal{C}}^{\rho^E}_{per}(\mathbf{k}) = \frac{1}{4\mu^2 V}\varepsilon_{isl}(ik_s)\left(\widetilde{\sigma}^{int}_{lj}(\mathbf{k}) - \frac{v}{1+v}\delta_{lj}\widetilde{\sigma}^{int}_{mm}(\mathbf{k})\right) \times \varepsilon_{jpq}(-ik_p)\left(\widetilde{\sigma}^{int}_{qi}(-\mathbf{k}) - \frac{v}{1+v}\delta_{qi}\widetilde{\sigma}^{int}_{nn}(-\mathbf{k})\right)$$

$$= \frac{k^2}{4\mu^2}\left(\frac{1}{V}\widetilde{\sigma}^{int}_{lj}(\mathbf{k})\widetilde{\sigma}^{int}_{lj}(-\mathbf{k})\right) - \frac{(1+v^2)k^2}{4\mu^2(1+v)^2}\left(\frac{1}{V}\widetilde{\sigma}^{int}_{mm}(\mathbf{k})\widetilde{\sigma}^{int}_{nn}(-\mathbf{k})\right),$$ (E.24)

where we make use of the equilibrium condition $\partial_i\sigma_{ij} = 0$ and thus $k_i\widetilde{\sigma}_{ij} = 0$. Substituting Eqs. (E.9) and (E.10) into Eqs. (E.23) and (E.24)

$$\widetilde{\mathcal{C}}^{\rho^E}_{tot}(\mathbf{k}) = \frac{k^2}{4\mu^2}\left[\widetilde{\mathcal{C}}^{\sigma}_{tot}(\mathbf{k}) - \frac{2v}{(1+v)^2}\widetilde{\mathcal{C}}^{\sigma}_{tr}(\mathbf{k})\right],$$ (E.25)

$$\widetilde{\mathcal{C}}^{\rho^E}_{per}(\mathbf{k}) = \frac{k^2}{4\mu^2}\left[\widetilde{\mathcal{C}}^{\sigma}_{tot}(\mathbf{k}) - \frac{1+v^2}{(1+v)^2}\widetilde{\mathcal{C}}^{\sigma}_{tr}(\mathbf{k})\right].$$ (E.26)

Here we can ignore the angle dependence if the stress-stress correlation functions are isotropic.

E.5. Scaling relations

According to Eq. (E.17), the term k^{d-1} suggests that the power-law exponent relation between E and $\widetilde{\mathcal{C}}^{\sigma}$ is

$$\gamma' = \gamma + d - 1.$$ (E.27)

Again, both Eqs. (E.23) and (E.24) imply that the power-law exponent relation between $\widetilde{\mathcal{C}}^{\rho^E}$ and $\widetilde{\mathcal{C}}^{\sigma}$ is

$$\gamma'' = \gamma + 2,$$ (E.28)

regardless of the dimension.

Table E.3 shows a nice agreement between predicted scaling and numerical measurements for power-law exponents of $\widetilde{\mathcal{C}}^{\sigma}, E,$ and $\widetilde{\mathcal{C}}^{\rho^E}$. These relations are valid in the presence of residual stress.

During the relaxation processes, the elastic free energy follows a power-law decay in time asymptotically, seen in Fig. 6. All the above measured correlation functions of elastic quantities share the same power laws in Fourier space, albeit with decaying magnitudes in time.

Table E.3
Power-laws relations among $\widetilde{\mathcal{C}}^{\sigma}(k)$, $E(k)$, and $\widetilde{\mathcal{C}}^{\rho^E}(k)$. (d represents the dimension; P.Q. and S.T. represent 'Physical Quantities' and 'Scaling Theory', respectively.)

C.F.	S.T.	Simulations					
		Climb and glide		Glide only (MDP)		LVP glide only (LVP)	
		2D (1024²)	3D (128³)	2D (1024²)	3D (128³)	2D (1024²)	3D (128³)
$\widetilde{C}^{\sigma}_{tot}(k)$	γ	−2.65	−3.1	−1.65	−3.0	−1.95	−3.1
$\widetilde{C}^{\sigma}_{tr}(k)$	γ	−2.65	−2.9	−1.65	−3.0	−1.95	−2.9
$E(k)$	$\gamma + d - 1$	−1.65	−1.1	−0.65	−1.0	−0.95	−1.1
$\widetilde{C}^{\rho^E}_{tot}(k)$	$\gamma + 2$	−0.65	−1.0	0.45	−1.0	−0.05	−1.0
$\widetilde{C}^{\rho^E}_{per}(k)$	$\gamma + 2$	−0.65	−1.0	0.45	−1.0	−0.05	−0.9

Y.S. Chen et al./International Journal of Plasticity 46 (2013) 94–129

References

Acharya, A., 2001. A model of crystal plasticity based on the theory of continuously distributed dislocations. J. Mech. Phys. Solids 49, 761–784.
Acharya, A., 2003. Driving forces and boundary conditions in continuum dislocation mechanics. Proc. R. Soc. A 459, 1343–1363.
Acharya, A., 2004. Constitutive analysis of finite deformation field dislocation mechanics. J. Mech. Phys. Solids 52, 301–316.
Acharya, A., 2011. Microcanonical entropy and mesoscale dislocation mechanics and plasticity. J. Elast. 104, 23–44.
Acharya, A., 2012. Private communication.
Acharya, A., Roy, A., 2006. Size effects and idealized dislocation microstructure at small scales: predictions of a phenomenological model of mesoscopic field dislocation mechanics: Part I. J. Mech. Phys. Solids 54, 1687–1710.
Acharya, A., Tartar, L., 2011. Driving forces and boundary conditions in continuum dislocation mechanics. Bull. Ital. Math. Union 9 (IV), 409–444.
Ananthakrishna, G., 2007. Current theoretical approaches to collective behavior of dislocations. Phys. Rep. 440, 113–259.
Bakó, B., Groma, I., 1999. Computer simulations of a three-dimensional Ising ferromagnet with quenched disorder. Phys. Rev. B 60, 9228–9231.
Bakó, B., Groma, I., Gyorgyi, G., Zimanyi, G.T., 2007. Dislocation glasses: aging during relaxation and coarsening. Phys. Rev. Lett. 98, 075701.
Bakó, B., Hoffelner, W., 2007. Cellular dislocation patterning during plastic deformation. Phys. Rev. B 76, 214108.
Chaikin, P., Lubensky, T., 1995. Principles of Condensed Matter Physics. Cambridge University Press, Cambridge, England.
Chen, Y.S., Choi, W., Papanikolaou, S., Bierbaum, M., Sethna, J.P., 2012. Plasticity Tools, <http://www.lassp.cornell.edu/sethna/Plasticity/Tools/>.
Chen, Y.S., Choi, W., Papanikolaou, S., Sethna, J.P., 2010. Bending crystals: emergence of fractal dislocation structures. Phys. Rev. Lett. 105, 105501.
Choi, W., Chen, Y.S., Papanikolaou, S., Sethna, J.P., in preparation.
Choi, W., Chen, Y.S., Papanikolaou, S., Sethna, J.P., 2012b. Is dislocation flow turbulent in deformed crystals? Comput. Sci. Eng. 14 (1), 33–39.
Coles, P., Lucchin, F., 1995. Cosmology: The Origin and Evolution of Cosmic Structures. Wiley, Chichester, England.
Dimiduk, D.M., Woodward, C., LeSar, R., Uchic, M.D., 2006. Scale-free intermittent flow in crystal plasticity. Science 312, 1188–1190.
Durin, G., Zapperi, S., 2006. The Barkhausen effect. In: Bertotti, G., Mayergoyz, I. (Eds.), The Science of Hysteresis, vol. II. Elsevier, Amsterdam, The Netherlands, pp. 181–267.
Falk, M.L., Langer, J.S., 1998. Dynamics of viscoplastic deformation in amorphous solids. Phys. Rev. E 57, 7192–7205.
Forster, D., 1975. Hydrodynamic Fluctuations Broken Symmetry and Correlation Functions. Benjamin-Cummings, Reading, MA.
Friedman, N., Jennings, A.T., Tsekenis, G., Kim, J.Y., Tao, M., Uhl, J.T., Greer, J.R., Dahmen, K.A., 2012. Statistics of dislocation slip avalanches in nanosized single crystals show tuned critical behavior predicted by a simple mean field model. Phys. Rev. Lett. 109, 095507.
Gil Sevillano, J., 1993. Patterns in heavily deformed metals. Scr. T49B, 405–411.
Gil Sevillano, J., Bouchaud, E., Kubin, L.P., 1991. The fractal nature of gliding dislocation lines. Scr. Metall. Mater. 25, 355–360.
Godfrey, A., Hughes, D.A., 2000. Scaling of the spacing of deformation induced dislocation boundaries. Acta Mater. 48, 1897–1905.
Gomez-Garcia, D., Devincre, B., Kubin, L.P., 2006. Dislocation patterns and the similitude principle: 2.5 D mesoscale simulations. Phys. Rev. Lett. 96, 125503.
Groma, I., Bakó, B., 2000. Dislocation patterning: from micro- to mesoscale description. Phys. Rev. Lett. 84, 1487–1490.
Hähner, P., 1996. On the foundations of stochastic dislocation dynamics. Appl. Phys. A 62, 473–481.
Hähner, P., Bay, K., Zaiser, M., 1998. Fractal dislocation patterning during plastic deformation. Phys. Rev. Lett. 81, 2470–2473.
Hansen, N., Huang, X., Winther, G., 2011. Effect of grain boundaries and grain orientation on structure and properties. Metall. Mater. Trans. A 42, 613–625.
Hirth, J.P., Lothe, J., 1982. Theory of Dislocations. Wiley, New York.
Hohenberg, P.C., Halperin, B.I., 1977. Theory of dynamic critical phenomena. Rev. Mod. Phys. 49, 435–479.
Hughes, D.A., Chrzan, D.C., Liu, Q., Hansen, N., 1998. Scaling of misorientation angle distributions. Phys. Rev. Lett. 81, 4664–4667.
Hughes, D.A., Hansen, N., 1993. Microstructural evolution in nickel during rolling from intermediate to large strains. Metall. Trans. A 24, 2022–2037.
Hughes, D.A., Hansen, N., 2001. Graded nanostructures produced by sliding and exhibiting universal behavior. Phys. Rev. Lett. 87, 135503.
Hughes, D.A., Liu, Q., Chrzan, D.C., Hansen, N., 1997. Scaling of microstructural parameters: misorientations of deformation induced boundaries. Acta Mater. 45, 105–112.
Kacher, J., Robertson, I., Nowell, M., Knapp, J., Hattar, K., 2011. Study of rapid grain boundary migration in a nanocrystalline ni thin film. Mater. Sci. Eng. A 528, 1628–1635.
Kawasaki, Y., Takeuchi, T., 1980. Cell structures in copper single-crystals deformed in the [001] and [111] axes. Scr. Metall. 14, 183–188.
Kiener, D., Guruprasad, P.J., Keralavarma, S.M., Dehm, G., Benzerga, A.A., 2011. Work hardening in micropillar compression: in situ experiments and modeling. Acta Mater. 59, 3825–3840.
Kosevich, A.M., 1979. Crystal dislocations and the theory of elasticity. In: Nabarro, F.N.R., Duesbery, M.S. (Eds.), Dislocations in Solids, vol. 1. North-Holland, Amsterdam, pp. 33–165.
Kröner, 1981. Continuum theory of defects. In: Balian, R., Kleman, M., Poirier, J.P. (Eds.), Physics of Defects, Les Houches, Session XXXV, 1980. North-Holland, Amsterdam, pp. 215–315.
Kröner, E., 1958. Kontinuumstheorie der Versetzungen und Eigenspannungen. Springer, Berlin, Germany.
Kuhlmann-Wilsdorf, D., 1985. Theory of workhardening 1934–1984. Metall. Mater. Trans. A 16, 2091–2108.
Kuhlmann-Wilsdorf, D., 1987. Leds: properties and effects of low energy dislocation structures. Mater. Sci. Eng. 86, 53–66.
Kuhlmann-Wilsdorf, D., Hansen, N., 1991. Geometrically necessary, incidental and subgrain boundaries. Scr. Metall. Mater. 25, 1557–1562.
Kurganov, A., Noelle, S., Petrova, G., 2001. Semidiscrete central-upwind schemes for hyperbolic conservation laws and Hamilton–Jacobi equations. SIAM J. Sci. Comput. 23, 707–740.
Landau, L.D., Lifshitz, E.M., 1970. Theory of Elasticity. second ed.. Pergamon Press, New York.
Lazar, M., 2011. On the fundamentals of the three-dimensional translation gauge theory of dislocations. Math. Mech. Solids 16, 253–264.
Limkumnerd, S., 2006. Mesoscale theory of grains and cells: polycrystals & plasticity. Ph.D. Thesis, Cornell University.
Limkumnerd, S., Sethna, J.P., 2006. Mesoscale theory of grains and cells: crystal plasticity and coarsening. Phys. Rev. Lett. 96, 095503.
Limkumnerd, S., Sethna, J.P., 2007. Stress-free states of continuum dislocation fields: rotations, grain boundaries, and the nye dislocation density tensor. Phys. Rev. B 75, 224121.
Limkumnerd, S., Sethna, J.P., 2008. Shocks and slip systems: predictions from a mesoscale theory of continuum dislocation dynamics. J. Mech. Phys. Solids 56, 1450–1459.
Liu, Q., 1994. A new method for determining the normals to planar structures and their trace directions in transmission electron microscopy. J. Appl. Cryst. 27, 762–766.
Lopes, A.B., Barlat, F., Gracio, J.J., Ferreira Duarte, J.F., Rauch, E.F., 2003. Effect of texture and microstructure on strain hardening anisotropy for aluminum deformed in uniaxial tension and simple shear. Int. J. Plast. 19, 1–22.
L'vov, V., 1991. Scale invariant theory of fully developed hydrodynamic turbulence-Hamiltonian approach. Phys. Rep. 207, 1–47.
Mach, J., Beaudoin, A.J., Acharya, A., 2010. Continuity in the plastic strain rate and its influence on texture evolution. J. Mech. Phys. Solids 58, 105–128.
Madec, R., Devincre, B., Kubin, L.P., 2002. Simulation of dislocation patterns in multislip. Scr. Mater. 47, 689–695.
Martin, P.C., 1968. Measurements and correlation functions. In: de Witt, C., Balian, R. (Eds.), Many-Body Physics. Gordon and Breach, New York, pp. 37–136.
Miguel, M.C., Vespignani, A., Zapperi, S., Weiss, J., Grasso, J.R., 2001. Intermittent dislocation flow in viscoplastic deformation. Nature 410, 667–671.
Mika, D.P., Dawson, P.R., 1999. Polycrystal plasticity modeling of intracrystalline boundary textures. Acta Mater. 47, 1355–1369.
Mughrabi, H., Ungar, T., Kienle, W., Wilkens, M., 1986. Long-range internal-stresses and asymmetric x-ray line-broadening in tensile-deformed [001]-orientated copper single-crystals. Philos. Mag. A 53, 793–813.
Mura, T., 1991. Micromechanics of Defects in Solids. second ed.. Kluwer Academic Publishers, Dordrecht, The Netherlands.
Nye, J.F., 1953. Some geometrical relations in dislocated crystals. Acta Metall. 1, 153–162.

Pantleon, W., 1996. On the distribution function of disorientations in dislocation cell structures. Scr. Metall. 35, 511–516.
Pantleon, W., 1998. On the statistical origin of disorientations in dislocation structures. Acta Mater. 46, 451–456.
Peebles, P.J.E., 1993. Principles of Physical Cosmology. Princeton University Press, Princeton, NJ.
Pumir, A., Siggia, E.D., 1992a. Development of singular solutions to the axisymmetric Euler equations. Phys. Fluids A 4, 1472–1491.
Pumir, A., Siggia, E.D., 1992b. Finite-time singularities in the axisymmetrical 3-dimension Euler equations. Phys. Rev. Lett. 68, 1511–1514.
Rickman, J.M., Viñals, J., 1997. Modelling of dislocation structures in materials. Philos. Mag. A 75, 1251–1262.
Roy, A., Acharya, A., 2005. Finite element approximation of field dislocation mechanics. J. Mech. Phys. Solids 53, 143–170.
Roy, A., Acharya, A., 2006. Size effects and idealized dislocation microstructure at small scales: predictions of a phenomenological model of mesoscopic field dislocation mechanics: Part II. J. Mech. Phys. Solids 54, 1711–1743.
Rutenberg, A.D., Vollmayr-Lee, B.P., 1999. Anisotropic coarsening: grain shapes and nonuniversal persistence exponents. Phys. Rev. Lett. 83, 3772–3775.
Salman, O., Truskinovsky, L., 2012. On the critical nature of plastic flow: one and two dimensional models. Int. J. Eng. Sci. 59, 219–254.
Sandfeld, S., Hochrainer, T., Gumbsch, P., Zaiser, M., 2010. Numerical implementation of a 3D continuum theory of dislocation dynamics and application to micro-bending. Philos. Mag. 90, 3697–3728.
Saxlová, M., Kratochvil, J., Zatloukal, J., 1997. The model of formation and disintegration of vein dislocation structure. Mater. Sci. Eng. A 234, 205–208.
Schmitt, J.H., Fernandes, J.V., Gracio, J.J., Vieira, M.F., 1991. Plastic behavior of copper sheets during sequential tension tests. Mater. Sci. Eng. A 147, 143–154.
Schwink, C., 1992. Flow-stress dependence on cell geometry in single-crystals. Scr. Metall. Mater. 27, 963–968.
Sethna, J.P., 2006. Statistical mechanics: Entropy Order Parameters and Complexity. Oxford University Press, New York.
Sethna, J.P., Coffman, V.R., Demler, E., 2003. Scaling in plasticity-induced cell-boundary microstructure: fragmentation and rotational diffusion. Phys. Rev. B 67, 184107.
Sethna, J.P., Dahmen, K.A., Myers, C.R., 2001. Crackling noise. Nature 410, 242–250.
Song, C., Havlin, S., Makse, H.A., 2005. Self-similarity of complex networks. Nature 433, 392–395.
Uchic, M.D., Dimiduk, D.M., Florando, J.N., Nix, W.D., 2004. Sample dimensions influence strength and crystal plasticity. Science 305, 986–989.
Ungár, T., Tóth, L.S., Illy, J., Kovács, I., 1986. Dislocation structure and work hardening in polycrystalline ofhc copper rods deformed by torsion and tension. Acta Metall. 34, 1257–1267.
Varadhan, S., Beaudoin, A., Fressengeas, C., 2006. Coupling the dynamics of statistically distributed and excess dislocations. In: Proceedings of Science, SMPRI 2005. p. 004.
Vergassola, M., Dubrulle, B., Frisch, U., Noullez, A., 1994. Burgers' equation, devil's staircases and the mass distribution for large-scale structures. Astron. Astrophys. 289, 325–356.
Walgraef, D., Aifantis, E., 1985. On the formation and stability of dislocation patterns. I: one-dimensional considerations. Int. J. Eng. Sci. 23, 1351–1358.
Wert, J.A., Huang, X., Winther, G., Pantleon, W., Poulsen, H.F., 2007. Revealing deformation microstructures. Mater. Today 10, 24–32.
Zaiser, M., 2006. Scale invariance in plastic flow of crystalline solids. Adv. Phys. 55 (1-2), 185–245.
Zaiser, M., Bay, K., Hähner, P., 1999. Fractal analysis of deformation-induced dislocation patterns. Acta Mater. 47, 2463–2476.
Zapperi, S., Zaiser, M., 2011. Private communication.